The International Journal of Advanced Manufacturing Technology (2018) 99:2755–2776
https://doi.org/10.1007/s00170-018-2618-1

ORIGINAL ARTICLE

# A numerical investigation on the local mechanical behavior of a 316-L part during and after an EDM basic electrical discharge

Adnene Tlili [1] · Farhat Ghanem [1]

Received: 10 June 2018 / Accepted: 16 August 2018 / Published online: 13 September 2018


**Abstract**
This study proposes a novel numerical approach to elucidate the mechanical behavior of the EDMed layer during an electrical discharge and enhance the numerical prediction of the EDM-induced residual stresses and work hardening, through advances at the levels of models, loads, and boundary conditions. In this work, a single-pulse discharge was simulated using finite element method carried out in ABAQUS/Explicit code. A fully coupled thermomechanical consistent model was developed based on a hydrodynamic Gruneisen-type behavior for the hydrostatic part of the stress, coupled with a Johnson-Cook plasticity model that takes into account a strain-rate-dependent stress in the range of a shockwave condition. A time-dependent heat source and pressure pulse are concurrently applied on the workpiece-loaded boundary. Numerical results highlighted relevant findings, especially the pre-eminence of the uniform distribution of the heat flux to predict the in-depth residual stress profile and the evident effect of the plasma-induced pressure on the work hardening and less on the residual stresses.

**Keywords** EDM · Numerical simulation · Residual stresses · Electrical discharge · Work hardening

## 1 Introduction

Electrical discharge machining (EDM) is a non-conventional machining process with very-high-energy density and characterized by the total absence of contact between the tool and the workpiece. EDM is a competitive process to machine difficult-to-cut materials via successive electric discharges generated between the workpiece and the tool electrode immersed in a dielectric medium. Each electrical discharge produces a colossal amount of energy ($\sim 10^{17}$ W m$^{-2}$ [1]) that will be transmitted in part to the hot-spots located on either side of the two electrodes. A few microseconds later, the temperature exceeds the evaporation temperatures. Finally, when the spark collapses, a fraction of the molten material is removed and results in a crater that represents the typical mark on EDMed parts. Applying consecutive discharges and driving one electrode toward the other, erodes the workpiece gradually in a form complementary to that of the tool electrode.

✉ Adnene Tlili
tlili_adnene@yahoo.fr

[1] Université de Tunis, ENSIT, Laboratoire de Mécanique, Matériaux et Procédés, 5 Avenue Taha Hussein, 1008 Montfleury, Tunisia

The major drawback of the EDM process is its crucial effects on the surface integrity. In this respect, relevant studies [2–5] have revealed the existence of residual tensile stresses, high work hardening gradient, and wide networks of microcracks and microvoids within the EDM-affected layer, which led to a drastic decrease in the fatigue lifetime of machined parts.

Numerous publications have focused on the numerical prediction of the residual stresses induced by the EDM process [5–22] based on almost common assumptions summarized hereafter.

The typical method often adopted is to calculate thermal stresses during the heating and cooling phases and the last equilibrium reached is then considered the residual stress state. Thermal stresses are assumed to be exclusively conditioned by the temperature gradient [6, 9, 13, 17, 21, 22] and the probable metallurgical transformations [7, 15, 19]. The volume expansion induced by the solid-solid metallurgical transformations has been accounted for implicitly by manipulating the thermal expansion coefficient [7, 8, 15, 20].

Several studies [6, 7, 9, 13, 15, 18, 20–22] have chosen a weak coupling between the thermal calculation and the stress analysis so that the transient temperature distributions obtained from the thermal analysis are used as inputs in the thermal stress computation. Liu et al. [17] proposed a sequentially

coupled thermal-mechanical analysis in a massive discharge model. The maximum temperature generated by each discharge is held until all the discharges are completed, and then cooled down to room temperature simultaneously. The temperature history obtained in the equivalent cooling model served as a pre-defined temperature field for the thermal-mechanical analysis assuming that there is no heating-induced stress in the discharging stage. Mechanical analysis be it quasi-static or dynamic is not available in most studies [6, 8, 13, 15, 17, 18, 20, 21]. However, transient thermal analysis is broadly adopted, excepting Salah Nizar et al. [22] who proposed a steady thermal analysis. The heat flux is assumed uniform with a disk-shaped distribution, Ghanem et al. [21] and has been further tested with the Gaussian distribution in the work of Yadav et al. [6]. In more recent works [7–9, 13, 15, 17, 18, 20, 22], Gaussian heat-flux distribution is unanimously accepted with shape coefficient ranging from 2 to 4.5.

Most published studies [6, 9, 15, 17, 22] have opted for an elastic-perfectly-plastic behavior. Pérez et al. [20] used a hardening plasticity till 400 °C and a perfect plasticity beyond that. Ghanem et al. [21] used an elastoplastic behavior with bilinear isotropic hardening.

Single-pulse model is commonly used [6–9, 13, 15, 21, 22], except Liu et al. [17] who proposed a probabilistic method to simulate the massive stochastic discharges in EDM and Pérez et al. [20] who simulated a second discharge on a sample already submitted to a single discharge.

The 2D axisymmetric model is commonly adopted because it provides good accuracy for a reasonable computation time. However, Meenakshi and Swee-Hock [7], Shabgard et al. [15], and Liu et al. [17] preferred a 3D model. Pradhan [13] treated the domain as semi-infinite object considering the microcosmic characteristics of the single discharge.

According to the studies cited above, thermal and metallurgical expansions are the main phenomena giving rise to thermal stresses. However, other studies have revealed the existence of additional phenomena that establish another kind of load which can potentially act simultaneously with thermal load.

Guo et al. [23] studied the mechanisms of material removal and crater formation in micro-EDM through molecular dynamics simulation of a model built using atomistic-continuum modeling method. They concluded that at the beginning of the discharge, material is removed as big clusters owing to the thermal shock effect which generates a stress wave, in the surface region, that propagates deeper into the cathode.

Yang et al. [24] investigated the residual stresses origin in micro-EDM process using the molecular dynamics method and the virial theory for the hydrostatic pressure distribution in melting area. The simulation results showed that after the discharge ignition, extremely high pressure (10 GPa) developed inside the melting area, the stress peaked at the boundary between the melting area and the solid region, and that the maximum normal stress was about − 13 GPa and the shear stress was about 3 GPa.

Yang et al. [25] analyzed the material removal mechanism in EDM using molecular dynamics simulation. They found that at the beginning of the discharge, the material is mainly removed by the superheated metal bubble explosion. Besides, a bulge shaped is observed around the discharge crater due to the shearing flow of the molten material caused by the high pressure generated in the workpiece beneath the discharge column, which creates a large pressure gradient in the superheated material.

Zhang et al. [26] simulated a single discharge in nano-EDM process by the combined atomistic-continuum modeling method. Based on this computational simulation model, the material is overheated and ultra-high thermal compressive stress (higher than 4 GPa) arises in the heated region and almost spreads all over the target and gets relieved when the material melts.

Singh and Ghosh [27] state that the large potential drop in the thin sheath near the electrode creates a very strong electric field that induces a negative charge on the cathode surface. This negative charge is then pulled outwards by the electric field, which leads to a stress creation on and below the surface. Based on this theory, a thermoelectric model is proposed in order to estimate the electrostatic force acting on the workpiece surface and the stresses induced inside the metal.

Yue and Yang [28] used the molecular dynamics method to simulate the material removal process caused by a single-pulse discharge in deionized water to elucidate the material removal motivity and mechanisms. They found that at the beginning of the discharge process, there exists an extremely high-pressure gradient along the depth direction toward the surface of the melting area. As the discharge continues, the range of the high pressure increases gradually up to 50 GPa, exceeding the atomic bonding forces. Thus, the electrode material is ablated, which relieves the pressure inside the melting area. Yue and Yang [28] also noticed that a high pressure (~ 10 GPa) still exists in the electrode after the discharge, and, hence, much material still can be removed.

In a similar study, Yue and Yang [29] mentioned the existence of a high pressure inside bubbles (~ 1250 MPa) whose expansions are impeded by the inertia and the viscosity of the dielectric liquid around them. Moreover, after the discharge, the pressure inside the bubbles was still high (~ 242 MPa).

Despite the limitation of computational capabilities and the spatiotemporal scale used, the molecular dynamics simulations provided an effective method to qualitatively study and investigate some new complex material-removal mechanisms in EDM processes that were experimentally confirmed by Hayakawa et al. [30].

These studies [23–29] confirm the existence of a pressure load and its related shockwave. The ultra-rapid propagation of

the shockwave inside the workpiece material indisputably affects its dynamic behavior and potentially generates work hardening and plastic deformations. This is indeed the phenomenon on which the laser shot peening process (LSP) is based. This process consists in inducing a purely mechanical effect in a material from the relaxation of a plasma generated on its surface by pulsed laser radiation [31–34]. According to these studies, the laser energy is absorbed in a very thin layer (~ 1 μm) of the target, which causes a direct ablation of the surface and consequently a plasma formation. Through the plasma-expansion-induced pressure, two shockwaves are emitted simultaneously, one in return in the air and the second toward the surface of the target. Using a dielectric confinement medium, the hydrodynamic expansion of the plasma is restricted by the inertia of the confinement medium which significantly amplifies the pressure-pulse magnitude and extends its duration.

Zhang et al. [35] have concluded the same thing in the case of EDM process. They found that the peak value of the impulsive force acting on the workpiece due to the expansion and contraction of the electric discharge-generated bubble were much higher in liquid dielectrics than in gaseous dielectrics.

The purpose of this study is to establish reliable models and assumptions through a numerical investigation and advances at the level of models and boundary conditions to elucidate the mechanical behavior of the EDMed layer during and after sparking and to enhance the numerical prediction of the residual mechanical state induced by EDM process.

In this work, a single-pulse discharge was simulated using finite element method carried out in ABAQUS/Explicit code, which is specifically devoted to dynamic analysis. A fully coupled thermomechanical consistent model is proposed based on a hydrodynamic Gruneisen-type behavior for the hydrostatic part of the stress, coupled with a Johnson-Cook plasticity model that takes into account a strain-rate-dependent stress in the range of $10^{-2}$ $s^{-1}$ (quasi-static load) to $10^{6}$ $s^{-1}$ (shockwave condition). A time-dependent heat source and pressure pulse were concurrently applied as boundary loads on the workpiece.

This paper is structured as follows. In Sect. 2, the modeling method is reviewed and details of the models are explained. Section 3 presents experimental setup and analysis of the results. In Sect. 4, the simulation results and analysis are reviewed, and then a discussion is made.

## 2 Modeling method and details

### 2.1 Thermal model

EDM is, basically, a thermal process, where the spark energy is transmitted to the electrodes through interaction between plasma and mater [36] via three mechanisms. The first mechanism is the positive ion bombardment which transmits their kinetic energy to the cathode spot. The second one is the high current densities in the hot-spot region, which leads to the Joule heating phenomenon. The third mechanism is the heat conduction and radiation from the high plasma temperature in front of the cathode spot [36–39].

The contribution of the Joule heating during an electrical discharge is extremely difficult to quantify experimentally since it is impossible to isolate it from the heat generated by the ionic impacts. Thereby, most of the thermal models proposed in the literature neglect the heat generated inside the workpiece by the Joule phenomenon [12, 40] and assume only a plasma-induced boundary heat source.

#### 2.1.1 Heat-source model

The heat flux $Q$, incoming the workpiece due to the electric discharge, exhibits a time-based change and a spatial distribution over the discharge spot. The temporal change is mainly governed by the expansion phenomenon of the heat source and less by the current pulse shape. The form of the heat flux distribution is a key factor that significantly affects the simulation results even with the same discharge energy and plasma diameter [41].

The Gaussian-shape distribution has recently become the most-cited model to approximate the distribution of the heat flux at the cathode [36, 41–49]. Kitamura and Kunieda [38] clarified the Gaussian-shape origin in their study on EDM gap phenomena using transparent SiC and $Ga_2O_3$ single crystal electrodes. They concluded that the heat flux is not uniform in the plasma and that the heat-source diameter is smaller than the plasma diameter since the distribution of the current density is narrower than that of plasma temperature broadening. However, other researchers still consider that the uniform distribution is a real hypothesis, capable of providing good results.

In this context, Kojima et al. [50] have experimentally measured the temperature evolution within the plasma channel. They concluded that the temperature is already higher than 5000 K right after dielectric breakdown and remains almost constant during discharge duration. They also find that the temperature is almost uniform along the plasma radial direction. Therefore, they sustain the presumption of a uniform distribution of the heat flux. Escobar et al. [51] compared three distribution patterns of the heat flux: point, uniform, and Gaussian. They found that uniform distribution led to good results. Maradia et al. [40] assumed a uniform heat-flux distribution on the cathode, and the numerical results showed a good agreement with the experimental measurements.

A circular heat source is applied in this study with two distribution alternatives namely uniform and Gaussian, to assess their impacts on the residual mechanical state.

In the case of Gaussian distribution, the heat flux density $Q_G$ is given by Eq. (1) [43, 46].

$$Q_G(r,t) = Q_0(t) \times \exp\left(-4.5 \times \left(\frac{r}{R(t)}\right)^2\right) \quad (1)$$

with:

$$Q_0(t) = \frac{4.57 \times U \times I(t) \times F_c}{\pi \times R(t)^2} \quad (2)$$

When applying a uniform distribution, the heat flux density $Q_U$ is given by Eq. (3):

$$Q_U(r,t) = Q_0(t) \times H(R(t)-r) \quad (3)$$

with:

$$Q_0(t) = \frac{U \times I(t) \times F_c}{\pi \times R(t)^2} \quad (4)$$

where $U$ and $I(t)$ are the discharge voltage and current, respectively, $r$ is the radial distance from the plasma axis, $Q_0(t)$ is the heat flux at the plasma axis, $R(t)$ is the time-dependent heat-source radius, $H(x)$ is the Heaviside function and $F_c$ is the fraction of energy transferred to the cathode.

#### 2.1.2 Fraction $F_c$

The amount of energy transferred to the cathode is an important factor, and its value remains a challenging issue of high complexity. This factor depends on several parameters such as the electrodes materials and the process conditions [40]. Several studies [40, 49, 52–56] suggest empirical values in the range of 6 to 60% for the cathode. In this study, two levels were examined that are 18% often used with the Gaussian heat flux distribution [41–44] and 45% as it was found to be a reliable assumption [56] and so used by Maradia et al. [40] in the case of a disc heat source.

#### 2.1.3 Discharge current function

As defined in Eqs. (1) and (3), the heat source becomes infinite when the discharge time is in the nanosecond regime. To avoid this numerical singularity, Guo et al. [44] proposed to express the current pulse by three functions that are activated sequentially to meet the natural profile of the signal during an electrical discharge.

In this study, the electrical discharge signal is assumed to follow a linear interpolation (Fig. 1) as following:

$$\begin{cases} I(t) = K_1 \cdot t, & t \in [0, t_1] \\ I(t) = I_{max}, & t \in [t_1, t_2] \\ I(t) = I_{max} - (K_1 \cdot (t - t_2)), & t \in [t_2, t_{on}] \end{cases} \quad (5)$$

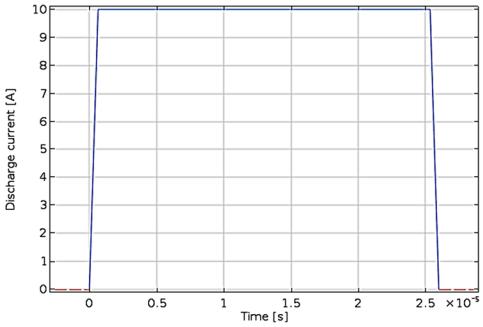


**Fig. 1** Linear interpolation of the current signal during discharge time

where $I(t)$ is the current at $t$ time, $t_{on}$ is the on-time of the discharge, $I_{max}$ is the discharge current, $K_1 = I_{max}/t_1 (A \cdot s^{-1})$, $t_1 = 2.5\% \times t_{on}$, $t_2 = t_{on} - t_1$.

#### 2.1.4 Heat-source expansion model

During an electrical discharge, the plasma expands and accordingly causes a perpetual decrease in the heat-flux density. Therefore, a consistent model for the heat-source expansion during discharge is a must have toward a better numerical transposal of the actual heat loading.

Numerous models have been proposed in the literature [38, 53, 54, 57, 58], and most of them are derived from inverse problem resolution based on the crater morphology and the material removal rate. Basically, these models can serve as an equivalent heat source rather than real plasma-expansion models.

Using spectroscopic measurement in EDM process, Kojima et al. [50] proved that plasma completes expanding within a few microseconds (~ 2 μs in air) after dielectric breakdown and then remains almost constant thereafter (~ 500 μm in air). This is in agreement with optical observations of Das et al. [8].

Shankar et al. [59] and Jilani et al. [60] studied the EDM plasma channel growth and reported that the discharge channel saturates beyond 20 μs when a dielectric liquid is used instead of air because the plasma expansion is delayed and restricted by the inertia of the dielectric liquid.

Based on these results, Liu and Guo [61] proposed a sequential plasma-expansion model in oil medium composed of a progression according to a power law up to a critical time (~ 100 μs) beyond which the plasma keeps a constant diameter (~ 240 μm).

Recently, Kitamura and Kunieda [38] have examined in situ the plasma expansion using transparent cathodes and a high-speed video camera. Their work resulted in two models, one that fits actual plasma expansion and the other that matches well the crater diameter. Table 1 summarizes the relevant equivalent heat source and plasma-expansion models.

The models proposed by Kitamura and Kunieda [38] will be assumed and examined in this study.

**Table 1** Relevant heat-source and plasma expansion models

| Model | | Ref. | Comment |
|---|---|---|---|
| Equivalent heat-source models | $R = 2.04\text{E}-03 \times I^{0.43} \times t^{0.44}$ | [58] | Valid for spark energy levels up to 670 (mj) |
| | $R_c = 0.0012 \times t^{0.331}$ | [20] | Crater expansion ($R_c$) |
| | $R_{bz} = 0.002 \times t^{0.295}$ | | Burned zone ($R_{bz}$) |
| | $R = \frac{(7.95\text{E}-03 \times t^{0.4})}{2}$ | [38] | Fits crater radius for both copper and steel anode |
| Plasma expansion models | $R = \frac{(2.5\text{E}-03 \times t^{0.18})}{2}$ | [38] | Fits plasma radius |
| | $R = 0.788 \times t^{0.75}$ | [52] | Recommended for small plasma radius (less than 5 μm) |
| | $R = \begin{cases} C_1 \times t^{0.75} & t \le t_c \\ C_2 & t > t_c \end{cases}$<br>$C_1 = 0.12$ (m s$^{-0.75}$)<br>$C_2 = 1.2\text{E}-04$ (m)<br>$T_c = 100$ (μs) | [61] | The stabilized plasma radius ($C_2$) and critical time ($t_c$) were estimated based on the experimental data of Kojima et al. [50] in the case of oil dielectric medium. |
| | $R = \begin{cases} C_1 \times t & t \le t_c \\ C_2 & t > t_c \end{cases}$<br>$C_1 = 125$ (m/s)<br>$C_2 = 2.5\text{E}-04$ (m)<br>$t_c = 2$ (μs) | [50] | Based on a single-pulse discharge ignited in air. |

The first model is of equivalent heat-source type (Eq. (6)):

$$R_1(t) = \frac{(7.95\text{E}{-}0.3 \times t^{0.4})}{2} \tag{6}$$

The second model is of plasma-expansion type (Eq. (7)) with a trend similar to that predicted by Kojima et al. [50], as shown in Fig. 2:

$$R_2(t) = \frac{(2.5\text{E}{-}03 \times t^{0.18})}{2} \tag{7}$$

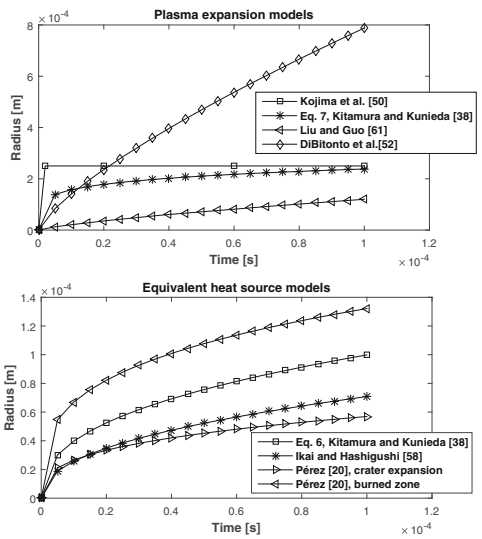


**Fig. 2** Time-based evolution of some plasma and equivalent heat-source expansion models

where $R_i(t)$ refers to the plasma radius (m) and $t$ is time (s).

#### 2.1.5 Heat diffusion

Given the necessary boundary conditions, the following heat diffusion equation can be solved to obtain the temperature distribution in the workpiece:

$$\rho C_p \frac{\partial T}{\partial t} = \nabla(K_t \nabla T) \tag{8}$$

Thermophysical properties of the workpiece material (density ($\rho$), heat capacity ($C_p$), and thermal conductivity ($K_t$)) are taken isotropic and temperature dependent.

An explicit method is used to account for the latent heat of fusion by changing $C_p$ in Eq. (8) by the effective specific heat defined as:

$$C_p^{\text{eff}} = C_p + \frac{L_{1\to2}}{\Delta T_{1\to2}} \tag{9}$$

where $L_{1\to2}$ is the latent heat from phases 1 to 2 and $\Delta T_{1\to2}$ is the temperature transition interval from phases 1 to 2.

Basic thermophysical properties, in solid state, of the austenitic stainless steel type AISI 316 [62] used in this study are listed in Table 2:

### 2.2 Mechanical model

Following the thermal load induced by the electrical discharge, the material expands locally proportionally to the

**Table 2** Thermophysical properties, in solid state, of the stainless-steel AISI 316L [62]

| | |
|---|---|
| Melting point (K) | 1703 |
| Boiling point (K) | 3090 |
| Latent heat of fusion (kJ $kg^{-1}$) | 270.0 |
| Density $\rho$ (kg $m^{-3}$) | $8084-(0.4209)\times T-(3.894E{-}05)\times T^2$ |
| Heat capacity $C_p$ J $Kg^{-1}$ $K^{-1}$ | $462+(0.134)\times T$ |
| Thermal conductivity $\lambda$ W $m^{-1}$ $K^{-1}$ | $9.248+(0.01571)\times T$ |
| Linear expansion coefficient $\alpha\times 1E{-}06$ ($K^{-1}$) | $17.89+(2.398E{-}03)\times T+(3.269E{-}07)\times T^2$ |

temperature. The thermal stresses and deformations are thus created and continue to evolve until reaching a final equilibrium state, often qualified by residual, once the part is completely cooled down. Some recent studies have revealed the existence of a pressure shock, of various backgrounds, which can potentially contribute to the deformation and hardening of the EDM affected layer.

In what follows, a modeling approach is developed that takes into account the pressure load induced by the EDM plasma.

#### 2.2.1 Material constitutive relation

During an electrical discharge which usually lasts a few tens of microseconds, the material in the hot spot and its vicinity experiences a very high strain rate ($\approx 10^5$ $s^{-1}$). At such strain rate, material exhibits a rate-dependent strain hardening. Therefore, the constitutive relations resulting from quasi-static case are no longer valid.

Dynamic yield stress at high strain rate can be derived from the Hugoniot elastic limit (HEL) defined by Eq. (10):

$$\sigma_y^{dyn}=\frac{1-2\nu}{1-\nu}\times \mathrm{HEL} \tag{10}$$

where HEL is the elastic limit in the direction of the shockwave propagation, $\nu$ is Poisson's ratio, and $\sigma_y^{dyn}$ is the dynamic yield stress.

A hydrodynamic behavior is assumed for the hydrostatic part of the stress coupled with a stress–strain mechanical relation for the deviatoric behavior. The hydrodynamic behavior is governed by *Mie–Grüneisen's* equation of state model (EOS) (Eq. (11)) which establishes a hydrostatic relationship between pressure ($P$) and internal energy ($E_m$) with reference to the material Hugoniot curve:

$$P=\frac{\rho_0\times C_0^2\times\eta}{(1-S\times\eta)^2}\times\left(1-\frac{\Gamma_0\times\eta}{2}\right)+\Gamma_0\times\rho_0\times E_m \tag{11}$$

where $P$ is the pressure, $\rho_0$ the initial density, $\Gamma_0$ the dimensionless *Grüneisen* coefficient in normal state, $C_0$ the speed of the sound, $\eta=1-(\rho_0/\rho)$, $E_m$ the internal energy per unit mass, and $S$ the linear Hugoniot slope coefficient between the wave velocity ($D$) and the particle velocity ($U$): $D=C_0+S\times U$.

*Grüneisen's* model parameters for the AISI 316L steel are presented in Table 3.

The deviatoric behavior is provided by the Johnson-Cook plasticity law with isotropic hardening. This model allows to account for the temperature effect and the stress-strain dependence at high strain rate between $\dot{\varepsilon}_0=10^{-2}$ $s^{-1}$ (quasi-static load) and $\dot{\varepsilon}_{eq}=10^6$ $s^{-1}$ (shock conditions) [63]. $\sigma_{eq}$ is given by:

$$\sigma_{eq}=\left(A+B\times\varepsilon_{eq}^n\right)\times\left(1+C\times\ln\left(\frac{\dot{\varepsilon}_{eq}}{\dot{\varepsilon}_0}\right)\right)\times\left(1-\left(\frac{T-T_r}{T_m-T_r}\right)^m\right) \tag{12}$$

where $\sigma_{eq}$ is the equivalent stress, $\varepsilon_{eq}$ is the equivalent plastic strain, $\dot{\varepsilon}_{eq}$ and $\dot{\varepsilon}_0$ are the strain rate and a reference strain rate, respectively, $A$, $B$, $n$, $C$, and $m$ are material constants, $T$ is the absolute temperature, $T_r$ is the room temperature, and $T_m$ is the melting temperature.

Johnson-Cook's parameters for the AISI 316L stainless steel are listed in Table 4. It should be mentioned that these values are valid until $10^5$ $s^{-1}$ of strain rate [63].

Table 5 shows Young's modulus as a function of temperature according to references [64, 65].

It is worth mentioning that Abaqus uses the shear modulus instead of Young's modulus when using EOS in the model.

In the case of isotropic materials, the shear modulus ($G$) is connected to Young's modulus ($E$) and to Poisson's coefficient ($\nu$) by the following expression (Eq. (13)) where $\nu$ is assumed to be 0.3:

$$G=\frac{E}{2(1+\nu)} \tag{13}$$

**Table 3** Grüneisen's model parameters for the stainless steel AISI 316L [31]

| $\rho_0$ (kg $m^{-3}$) | $C_0$ (m $s^{-1}$) | Cel (m $s^{-1}$) | S | HEL (MPa) | $\Gamma_0$ |
|---|---|---|---|---|---|
| 7900 | 4570 | 600 | 1.49 | 1100 | 2 |

**Table 4** Johnson-Cook's parameters for the stainless steel AISI 316L [31]

| A (MPa) | B (MPa) | C | n | m | $\dot{\varepsilon}_0$ ($s^{-1}$) | $T_m$ (K) |
|---|---|---|---|---|---|---|
| 300 | 600 | 0.045 | 0.35 | 0.5 | 1 | 1700 |

**Table 5** Young's modulus vs. temperature for the stainless steel AISI 316L [64, 65]

| $T$ (°C) | 20 | 100 | 200 | 300 | 400 | 500 | 600 | 700 | 800 | 900 | 1000 | 1100 | 1200 |
|---|---|---|---|---|---|---|---|---|---|---|---|---|---|
| $E$ (GPa) | 197 | 191.5 | 184 | 176.5 | 168 | 160 | 151.5 | 142.5 | 130 | 108 | 81.5 | 32 | 7.4 |

### 2.2.2 Pressure pulse model

A consistent pressure pulse model requires the knowledge of three important inputs that are the magnitude of the peak pressure, the temporal evolution of the pressure, and its spatial distribution.

To our knowledge, there are no published experimental measurements or reliable models in the EDM-related literature that can be used to characterize the pressure shock owing to the plasma-matter interaction in the case of EDM process. For this reason, reference is made to the available models in the field of LSP where the plasma-induced pressure is exhaustively studied and characterized [32, 34].

To compute the magnitude of the peak pressure as a function of the heat flux transmitted to the workpiece, we used the LSP-associated model (Eq. (14)) proposed by Sollier [66]. This model postulates that in confined plasma mode, the pressure is proportional to the square root of the incident laser power density.

$$P_0 = 1.7 \times \sqrt{I_0} \tag{14}$$

with $P_0$ (GPa) being the plasma-induced peak pressure and $I_0$ (GW $cm^{-2}$) the laser power density.

Peyre et al. [67] revealed that laser shot peening of a surface immersed in water causes an intensification (ranging from 5 to 10) of the shock amplitude by a trapping-like effect of the plasma.

In this paper, this model (Eq. 14) is adapted and applied in the case of EDM process. The laser power $I_0$ is substituted by the EDM heat flux at the plasma axis $Q_0(t)$. A factor $F_p$ is added to the model to take account of the pressure amplification phenomenon caused by the dielectric liquid often present in the EDM process. Since $Q_0(t)$ is time dependent, the pressure $P_0(t)$ too will be time dependent as expressed by the following equation:

$$P_0(t) = 1.7 \times F_p \times \sqrt{Q_0(t)} \tag{15}$$

The time-based profile of a laser-generated pressure pulse $p = f(t)$ is well identified in the LSP process for a given pulse duration and a laser power density (Fig. 3). It is always considered a quasi-Gaussian peak pressure. Yue and Yang [28] found numerically a similar behavior in the EDM process, as shown in Fig. 4.

In the case of the EDM process, this trend of pressure evolution is coherent with *Descoeudres's* [68] experimental measurements where he states that:

- The electron density is extremely high during the first microsecond of the discharge and decreases rapidly afterwards. The ion density is roughly equal to the electron density;
- The light emitted by the plasma is much more intense during the first microsecond than during the rest of the discharge;
- At the end of the discharge, the plasma implodes and disappears quickly;
- The plasma is of high density in the early stage of the discharge (above $10^{18}$ $cm^{-3}$) and then decreases during the discharge. But even after a few tens of microseconds, the electron density remains high, above $10^{16}$ $cm^{-3}$;
- During the whole discharge, the density measured is slightly higher in the plasma center.

Based on these findings, it was possible to establish the hypothesis that pressure reaches its peak in the first

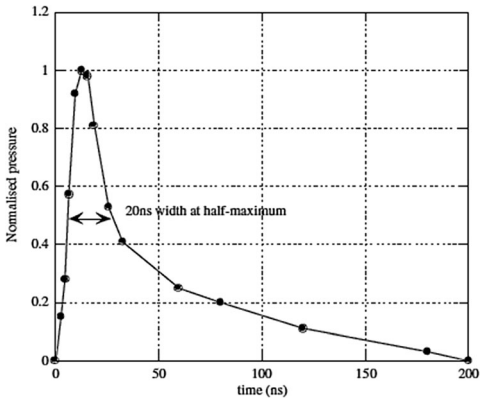


**Fig. 3** Normalized pressure pulse induced by 10 ns laser pulse in LSP process [31]

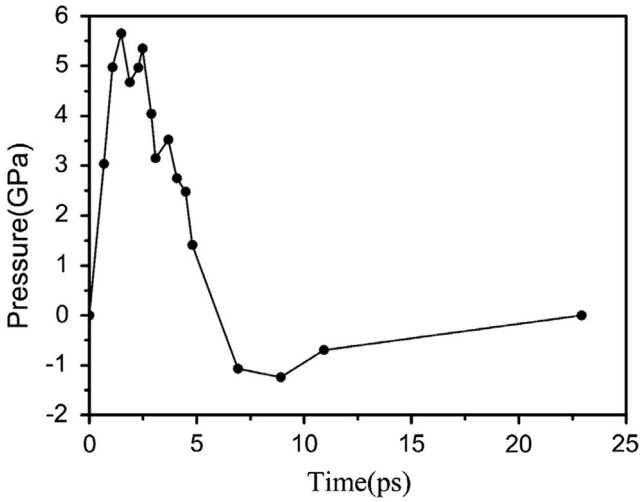


**Fig. 4** Average of pressure with respect to time in EDM process [28]

microseconds of the discharge, then decreases to almost 0 at the end of the on-time.

According to Eq. (15), the plot of the time-based evolution of the peak pressure (Fig. 5) at the plasma axis using factor $F_p = 5$ leads to a very similar trend to that presented in Fig. 3.

The spatial pressure distribution $P = f(r)$ is less easy to characterize. In the LSP process, the best experience/simulation match was found for a spherical-type distribution [32]. This optimized distribution (Eq. (16)) is used in this work. Given that the behavior of the EDM plasma is different from that in the LSP process, it was conceivable to examine also the uniform distribution of the pressure as expressed by Eq. (17):

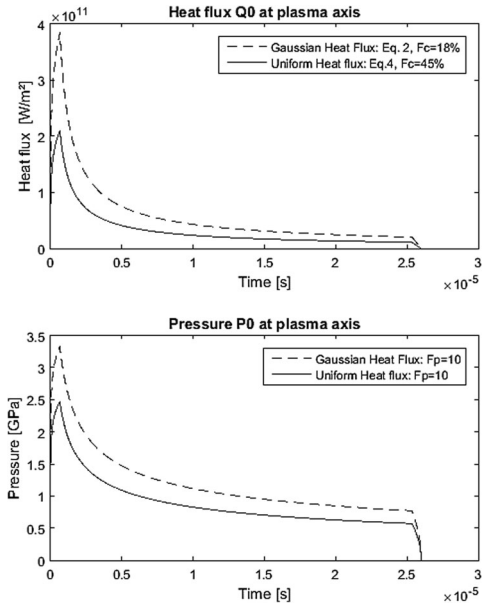


**Fig. 5** Top, heat flux density $Q_0(t)$ at plasma axis. Bottom, pressure $P0(t)$ at plasma axis. $U = 26$ V, $I = 10$ A, ton = 26 µs, $F_p = 10$, plasma expansion model Eq. (6)

$$P(r,t) = P_0(t) \times \sqrt{1 - \frac{0.5 \times r^2}{R(t)^2}} \tag{16}$$

$$P(r,t) = P_0(t) \times H(R(t) - r) \tag{17}$$

where $P(r,t)$ is the pressure magnitude, $P_0(t)$ is the peak pressure, and $R(t)$ is the time-dependent heat-source radius, $r$ is the radial distance from the plasma axis, and $H(x)$ is the Heaviside function.

## 2.3 Model design and mesh

The commercial code ABAQUS/Explicit was used to compute the stress and strain distribution on the EDMed workpiece, during and after a single electrical discharge. The problem is considered 2D semi-infinite axisymmetric with a domain shaped like a quarter disc (Fig. 6). Linear explicit-coupled temperature displacement CAX4RT elements (A four-node thermally coupled axisymmetric quadrilateral, bilinear displacement, and temperature, reduced integration, hourglass control) were allocated to the finite domain, with a denser mesh near the loaded boundary. A symmetric boundary condition was assigned to the (O, $y$) axis.

A CINAX4 infinite-element boundary is imposed in the model to avoid the reflection of the shockwaves on the free surface which ensure the stability and the convergence toward the equilibrium state. The FEM computation was performed in two dynamic analysis steps and carried out in ABAQUS/Explicit code to capture the material rapid response to a single electrical discharge. During the first

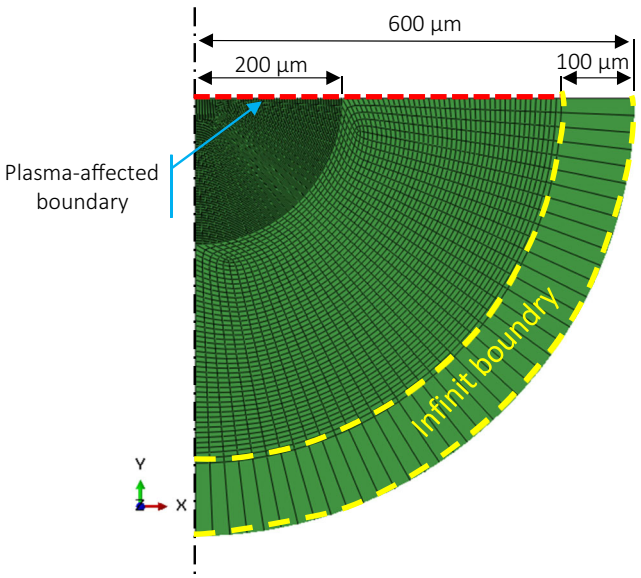


**Fig. 6** Schematic of axisymmetric model used in ABAQUS™: finite + infinite element model

step, a time-dependent heat flux and pressure pulse are submitted to the plasma-affected boundary, and forced convection is assigned beyond. The total step time is taken equal to the on-time 26 μs.

The second step is activated right after the first one, during which the cooling relaxation phase is simulated without any thermal and mechanical loading in order to compute the residual deformation and stress fields. Its time duration is taken long enough so as to reach room temperature and a quasi-steady equilibrium state whose stresses and deformations fields are considered quasi-residual. It is important to notice that we could have carried out the cooling relaxation step into ABAQUS/Implicit code, but we opted for an explicit formulation and used material damping to control numerical oscillations and to reach a quasi-residual stress field.

## 3 Experimental characterization of the EDM-affected layer

A series of experiments was carried out on AISI 316L square-shaped samples (workpiece) of 20 mm edge length, cut from 4-mm-thick plate and then machined on die-sinking electrical discharge machine (*Eurotech* BASIC 450) using graphite as tool electrode and a commercial EDM oil as dielectric fluid. The main machining parameters used are listed in Table 6.

The choice of these parameters is driven by the fact that low-energy discharges are used at the end of the EDM standard process and therefore, are responsible for the final surface integrity.

### 3.1 Residual stresses

Residual stress analysis was conducted by X-ray diffraction (XRD) according to the French standard AFNOR XP A 09-285 on May 1999. The classical "$\sin^2 \psi$" method was applied for the stress measurement with the use of 11 $\psi$-angles for each stress value. A special stress analysis system SET-X was used with {3 1 1} plane under $K_{\alpha 1}$ of Cr ($\lambda = 0.229$ nm). The analysis zone is limited by a collimator of 2 mm in diameter. Due to the weak penetration depth of X-ray radiation (about 5 μm with 66% absorption of the incident radiation), for each in-thickness stress measurement, a thin layer was removed by electropolishing techniques using a chlorine-based acid electrolyte. Then the X-ray diffraction measurements were carried out on the newly exposed surface located at a known depth below the original surface. To locally polish the workpiece, an adhesive mask was pasted on the sample to delimit an etching circle of 8 mm in diameter.

This procedure does not introduce additional stresses but relaxes already existing residual stresses. According to Belassel [33], the XRD results with the local polishing method can be considered valid when the removal depth is lower than one tenth the diameter for a cylindrical specimen. Beyond this value, the results should be corrected to account for the stress relaxation resulting from the local material removal. Belassel [33] also states that there is no reliable correction model available for this local removal technique.

The in-depth measurements of the residual stresses' normal components are shown in Fig. 7. In the first 100 μm close to the EDMed surface, tensile stresses are predominant and reach their maximum amplitude at 25 μm below the surface. Tensile stresses are then balanced by compressive stresses.

Shear stresses (Fig. 8) are significantly weaker than the normal stresses. The weakness of the shear stresses reveals the predominance of the voluminal expansion-based deformation of the matter, which highlights the isotropic nature of the residual stress field.

### 3.2 Work hardening

In addition to the tensile residual stresses, the EDM process induces a substantial work hardening gradient in the heat-

**Table 6** EDM machining parameters

| | |
|---|---|
| Discharge current $I$ (A) | 10 |
| Discharge voltage $U$ (V) | 26 |
| Pulse duration $t_{on}$ (μs) | 26 |
| Workpiece polarization | Cathode |

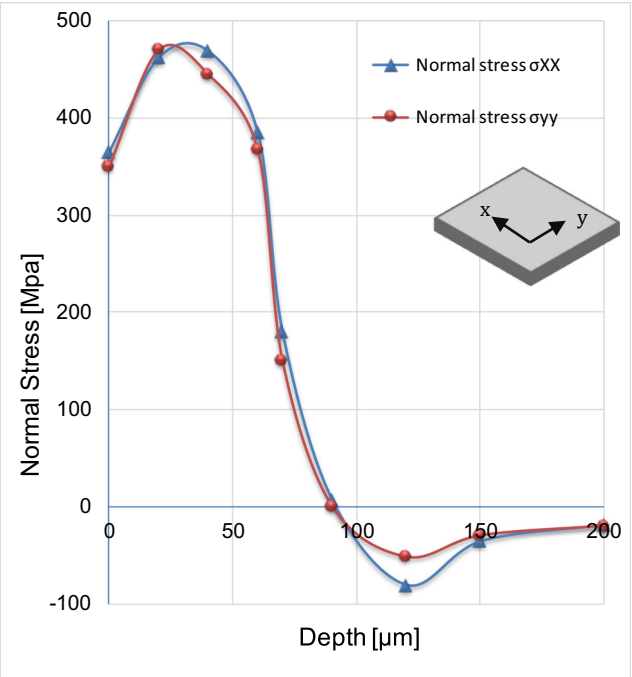


**Fig. 7** In-depth residual stress profiles for $\sigma_{xx}$ and $\sigma_{yy}$ components. $I$ = 10 A, ton = 26 μs

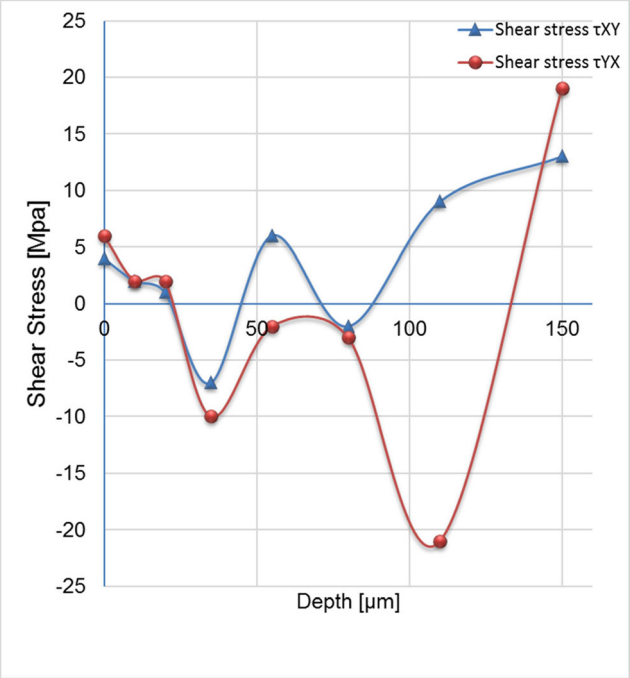


**Fig. 8** In-depth residual stress profiles, $\tau_{xy}$ and $\tau_{yx}$ components. $I = 10$ A, ton = 26 µs

affected layer that can be estimated by microhardness measurements and X-ray diffraction peak broadening [69].

#### 3.2.1 X-ray diffraction peak broadening

When a metallic material is machined by the EDM process, the crystals in the heat-affected layer are plastically deformed. As the crystals are deformed, lattice defects and dislocation tangles develop, producing microstrain (strain over the dimensions on the order of the crystal lattice) and a reduction in the crystallite size. Both the increase in microstrain and the reduction in the crystallite size cause broadening of the X-ray diffraction peak (integral width). The line-broadening data can be used to qualitatively assess the hardening level within the EDMed layer.

Figure 9 shows the in-depth X-ray diffraction peak broadening in EDMed sample. The curve decreases in-depth up to about 100 µm. It drops from 3.7°, at the top surface, to 2.28° at a depth of 100 µm. Beyond this limit, it remains almost constant, which indicates the beginning of the bulk material zone, undisturbed by the EDM process. Figure 9 highlights also the isotropy of the plastic deformation as confirmed by the in-depth integral width along X and Y orientations.

#### 3.2.2 Vickers microhardness tests

Microhardness measurements were carried out using a ©CSM micro-indentation tester according to the indentation

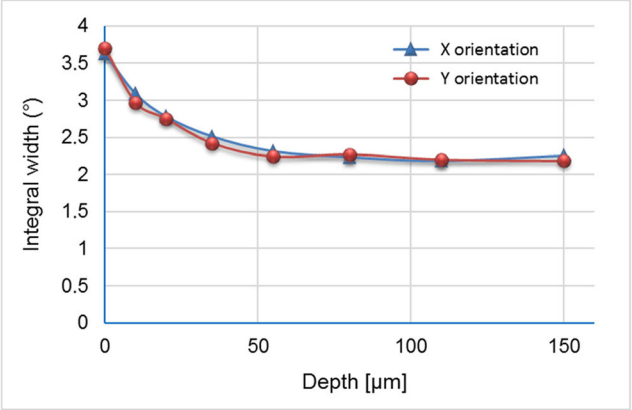


**Fig. 9** In-depth X-ray diffraction peak broadening. $I = 10$ A, ton = 26 µs

parameters presented in Table 7. The first measurement was taken at a depth of 15 µm to avoid the edge effect.

Figure 10 illustrates the in-depth microhardness measurements. The curve starts with the maximum recorded value of 520 HV located just beneath the EDMed surface and then decreases almost linearly up to 50 µm. finally, it stabilizes at a value of 230 HV (bulk material hardness).

The in-depth microhardness profile offers important qualitative information on the hardening state that prevails in the near-surface layers. Ben Moussa et al. [70] proposed an experimental-based curve correlating the equivalent plastic strain (EPS) to the microhardness HV measurements in the case of the AISI 316L stainless steel. Based on this curve, the equivalent plastic strain is evaluated in the EDMed layer, as shown in Fig. 10. It is worth mentioning that this quantification is to be considered with caution and serves only as an indication of the work hardening level.

At 15 µm below the EDMed surface, the level of the EPS is very high (~ 70%). Then, it decreases, almost linearly to stabilize at about 13%, which corresponds to the undisturbed bulk material. This percentage comes naturally from the rolling process of the sheet from which the samples are taken.

### 3.3 Element content change

The in-depth content change of the main chemical elements (carbon, iron, chromium, manganese, and molybdenum) was

**Table 7** Indentation parameters

| | |
|---|---|
| Approach speed | 25 (µm $min^{-1}$) |
| Acquisition rate | 10.0 (Hz) |
| Loading | Linear |
| Maximum load | 500.00 (mN) |
| Load speed | 1000.00 (mN $min^{-1}$) |
| Discharge speed | 1000.00 (mN $min^{-1}$) |
| Pause | 5.0 (s) |
| Type of indenter | Vickers |
| Indenter material | Diamond |

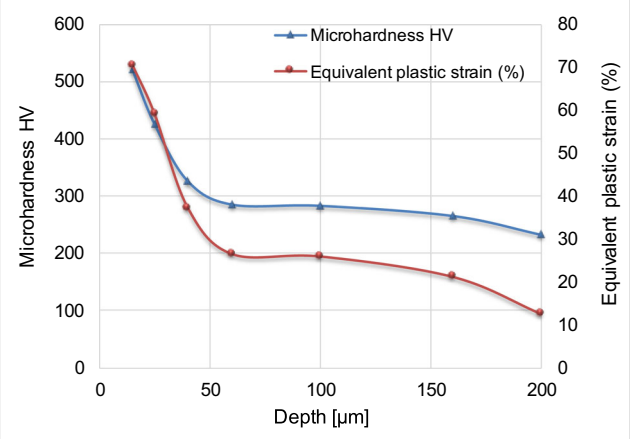


**Fig. 10** In-depth microhardness HV and equivalent plastic strain. $I = 10$ A, ton = 26 µs

investigated by means of energy-dispersive X-ray spectroscopy (EDS) on EDMed specimens. The analysis of the profiles (Fig. 11) clearly shows a carbon enrichment in the first 10 µm. This is mainly due to the diffusion phenomenon of carbon atoms coming from the dielectric liquid and the graphite of the tool.

## 4 Results and validation

Several combinations of hypotheses were tested, and those that gave the most relevant results are summarized in Table 8 and analyzed.

The form of the heat-flux distribution has significantly influenced the mechanical response of the EDMed layer. To emphasize the specificities inherent in each kind of distribution, the results have been gathered in two groups according to the form of the heat-flux distribution (HFD). Gaussian heat-flux distribution (GHFD) is assumed in the first group, while uniform heat-flux distribution (UHFD) in the second. Simulation results have been compared with experimental data from the current database.

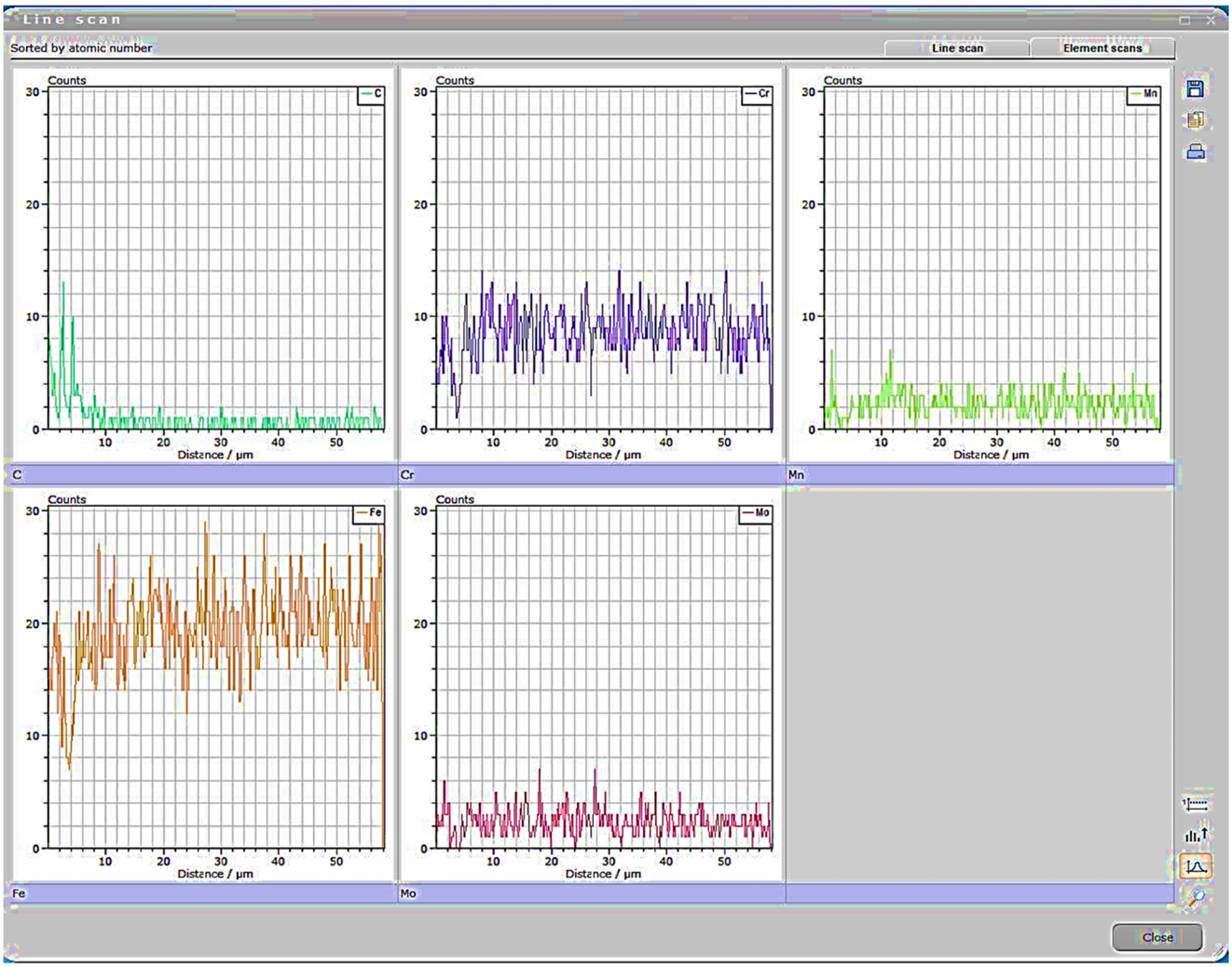


**Fig. 11** Energy-dispersive X-ray spectroscopy (EDS) line scan $I = 10$ A, ton = 26 µs

**Table 8** Summary of the conclusive combinations

| Combination | Thermal | | | | | | Mechanical | | | | | |
|---|---|---|---|---|---|---|---|---|---|---|---|---|
| | Heat-source radius | $F_c$ (%) | | Heat-flux distribution | | Heat-flux peak × E+11 (W m$^{-2}$) | Plasma radius | $F_p$ | | Pressure distribution | | Peak pressure (GPa) |
| | | 18 | 45 | Gaussian | Uniform | | | 10 | 15 | Spherical | Uniform | |
| C1 | Eq. (6) | × | | × | | 3.84 | Eq. (6) | 4 | | × | | 1.33 |
| C2 | | × | | × | | | | × | | | × | 3.33 |
| C3 | | × | | × | | | | | × | | × | 5 |
| C4 | | × | | × | | | | | | | | 0 |
| C5 | Eq. (6) | | × | | × | 2.1 | Eq. (6) | × | | | × | 2.46 |
| C6 | | | × | | × | | | | × | | × | 3.7 |
| C7 | | | × | | × | | | | | | | 0 |

## 4.1 Mechanical response of the EDM-affected layer

The elementary electric cycle on which the EDM process is based is consist of two critical phases. The first one is the discharge phase sustained for a period of on-time ($t_{on}$). The second is the pause time ($t_{off}$), which instantaneously occurs right after the first one when turning off the electric energy.

This electric cycle triggers a sequence of thermomechanical loadings, starting by a high energy heat flux and a pressure pulse, acting at once on the machined surface during the first phase, followed by a cooling stage during the second phase. The material reacts against these loadings and exhibits a particular behavior that is very interesting to know. The numerical model developed in this study allowed to follow the behavior of the workpiece throughout an EDM basic electrical-cycle.

### 4.1.1 Pure thermal loading (without pressure)

At the end of the heating phase, a pool of still molten matter located at the top layer exhibited a stress-free state. The extent of this area in terms of (radius, depth) is sensitive to the form used for the HFD. In the case of UHFD (Fig. 12a), it is (76 μm, 12 μm) against (44 μm, 14 μm) for the GHFD (Fig. 13a).

In the solid layer below the melting pool, reigns a field of compressive stresses which is less thick in the case of GHFD (Fig. 14a) but with more intense stresses (−110.2 MPa) than those developed by the UHFD (−47.3 MPa) (Fig. 14b). This compressed layer is then enveloped by a band of tensile stresses that balance the compression stresses.

The very high temperature in the hotspot causes a large thermal expansion of the molten material. This expansion, blocked by the cold sublayers, escapes through the surface of the workpiece that is free of any external pressure. This is noticeable especially for the model with GHFD (Fig. 13a) where a swelling is well developed on the surface. In the case of UHFD, the same phenomenon exists but as an uprising of the surface (Fig. 12a) rather than swelling.

At the end of the on-time, and whatever the form of the HFD, a zone of plastic deformations, developed in the solid sublayers, surrounds the molten pool. The Equivalent Plastic Strain (EPS) is slightly higher in the case of the GHFD (Fig. 15a) with a max = 8.46% against 7.48% for the UHFD (Fig. 15b) which has broader plastically

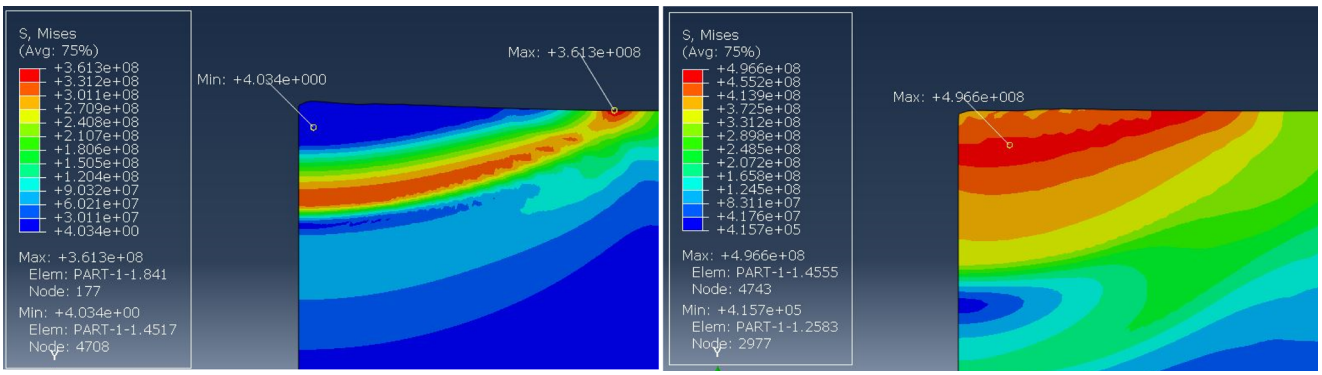


**Fig. 12** Mises stress fields in the case of pure thermal load with UHFD (combination C7): **a** at the end of the on-time and **b** after total cooling

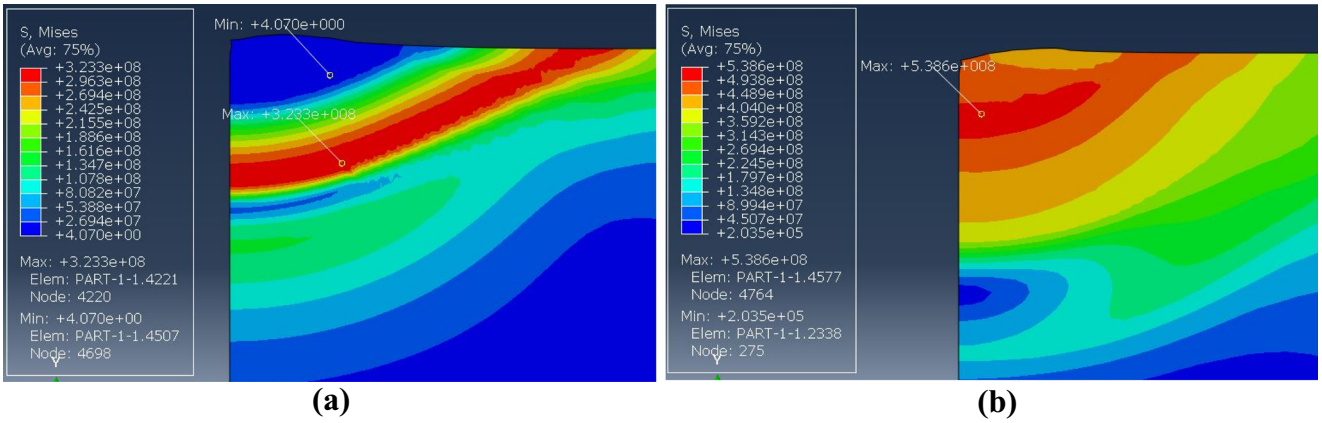


**Fig. 13** Mises stress fields in the case of pure thermal load with GHFD (combination C4) **a** at the end of the on-time and **b** after total cooling

deformed area caused by the uniform distribution of the heat flux that allows temperatures to diffuse further and reach deeper areas.

At the beginning of the cooling phase, the total mechanical strain rate remains high, particularly in the hot-spot. Ranging from 3.44E+04 $s^{-1}$ for the GHFD to 5.22E+04 $s^{-1}$ for the UHFD, as shown respectively in Fig. 16c, d.

During the cooling phase, the plastic deformation increases and develops further in depth and toward the surface to dominate the area that has solidified. The same behavior is detected in both cases of HFD and the maximum values reached in terms of EPS are very close (12 and 15%) as shown in Fig. 15c, d, respectively.

After total cooling, the workpiece reaches the room temperature and there appears a residual mechanical equilibrium state characterized by a gradient of residual stresses and work hardening. Figures 12b and 13b illustrate the residual Von-Mises stress in the case of a UHFD and GHFD, respectively.

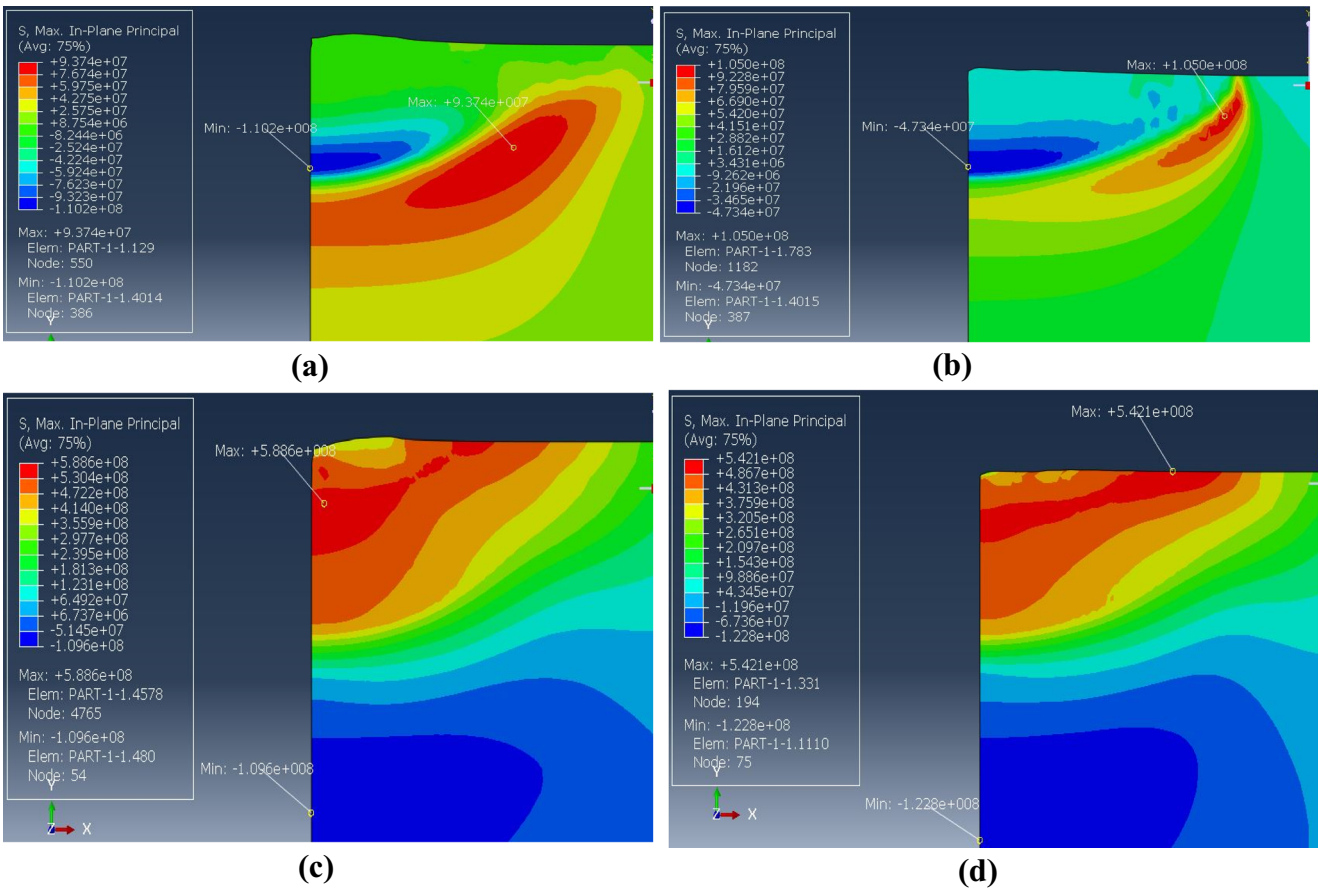


**Fig. 14** Max. in-plane principal, stress fields in the case of pure thermal load with combination C4 (GHFD) **a** at the end of the on-time and **c** after total cooling and combination C7 (UHFD) **b** at the end of the on-time and **d** after total cooling

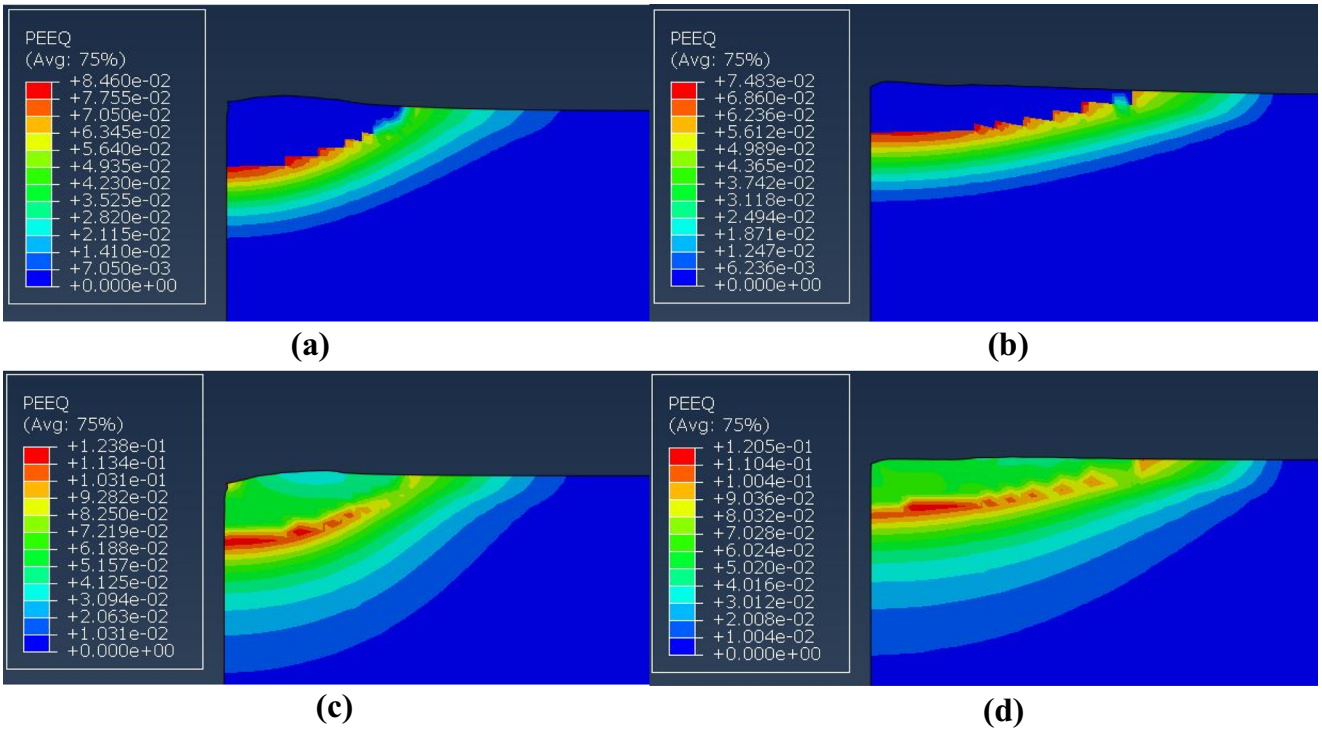


**Fig. 15** Equivalent plastic strain fields in the case of pure thermal load with combination C4 (GHFD) **a** at the end of the on-time and **c** after total cooling and combination C7 (UHFD) **b** at the end of the on-time and **d** after total cooling

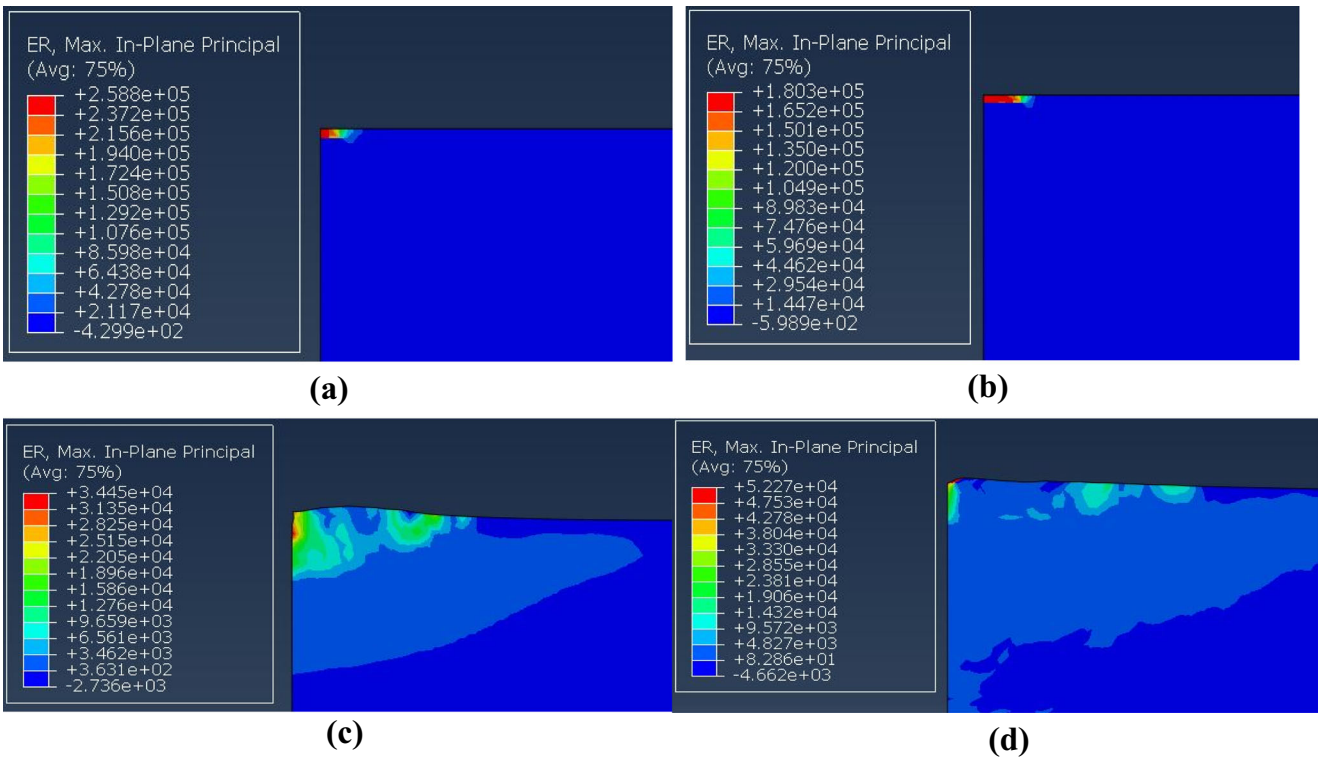


**Fig. 16** Max, in-plane principal, total mechanical strain rate fields in the case of pure thermal load with combination C4 (GHFD) **a** at 1E-07 μs and **c** at the end of the on-time and combination C7 (UHFD) **b** at 1E-07 μs and **d** at the end of the on-time

With the GHFD, the maximum of the stress amplitude is 538.6 MPa versus 496.6 MPa for the UHFD. Whatever the HFD, the maximum stress amplitudes are localized in sublayer in the form of a band which may extend up to the surface in the case of UHFD as shown in Fig. 12b.

The residual tensile stresses dominate the surface layers of 80 μm thick in the case of the UHFD (Fig. 14d) versus 64 μm for the GHFD (Fig. 14c).

#### 4.1.2 Thermal and pressure loads

When pressure is added as a load, the global aspect of the stress distribution in the workpiece remains roughly the same as shown in Fig. 17a–d. There is a general increase in the stress magnitude proportionately to the peak pressure applied. For a peak pressure of 5 GPa (combination C3), the maximum amplitude of the Mises stress reaches 642 MPa (Fig. 17b), whereas it was 538 MPa without the pressure (Fig. 13b). The same trend is detected also for the plastic deformation where an increase in peak pressure induces an increase in EPS, as shown in Fig. 18a–d.

The morphology of the crater is significantly different, depending on whether the pressure is applied or not. In the case of pure thermal loading, no crater shape is visible (Figs. 12b and Fig. 13b), while in all cases where the pressure is active, the presence of a crater shape is perfectly visible for all combinations considered under pressure, as shown in Fig. 17a–d.

### 4.2 Residual stresses validation

#### 4.2.1 Influence of the heat flux distribution

Two types of heat flux distributions have been tested. Figure 19 illustrates the influence of each distribution on the calculated residual stresses in the absence of any external pressure. The numerical profiles of residual stresses from the C4 and C7 combinations are similar in overall appearance to the experimental one. The residual stresses are of traction type on the surface, then balanced by compressive stresses in sublayers. Note also that the peak of tensile stresses is approximately 15 μm below the surface.

The C7 combination built on a UHFD allows a better prediction of the residual stresses when compared with the experimental measurements, especially at the magnitude level and the extent of the tensile stresses. However, an overvaluation of

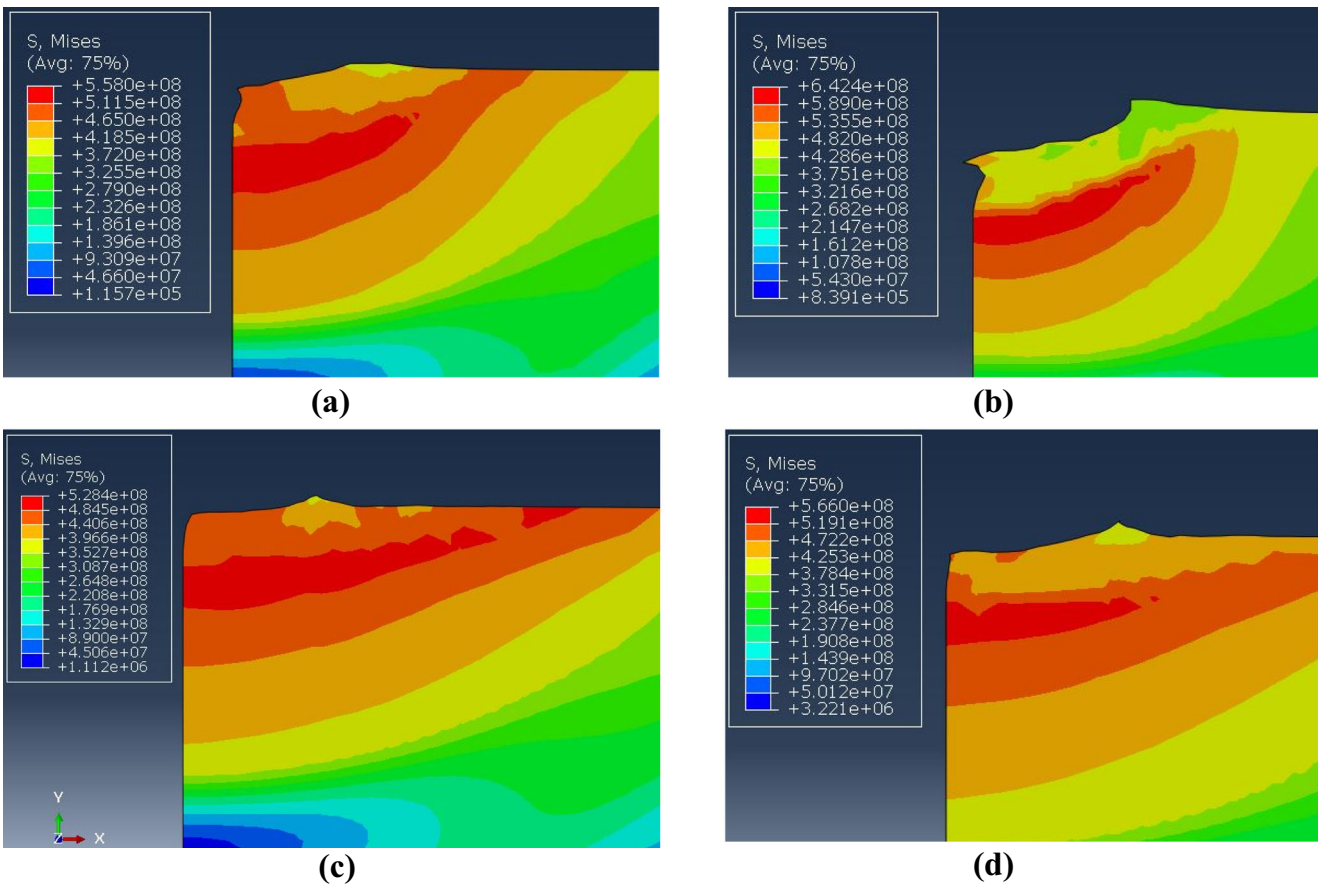


**Fig. 17** Mises stress fields after total cooling in the case of thermal and pressure loading. Combinations: **a** C2, **b** C3, **c** C5, and **d** C6

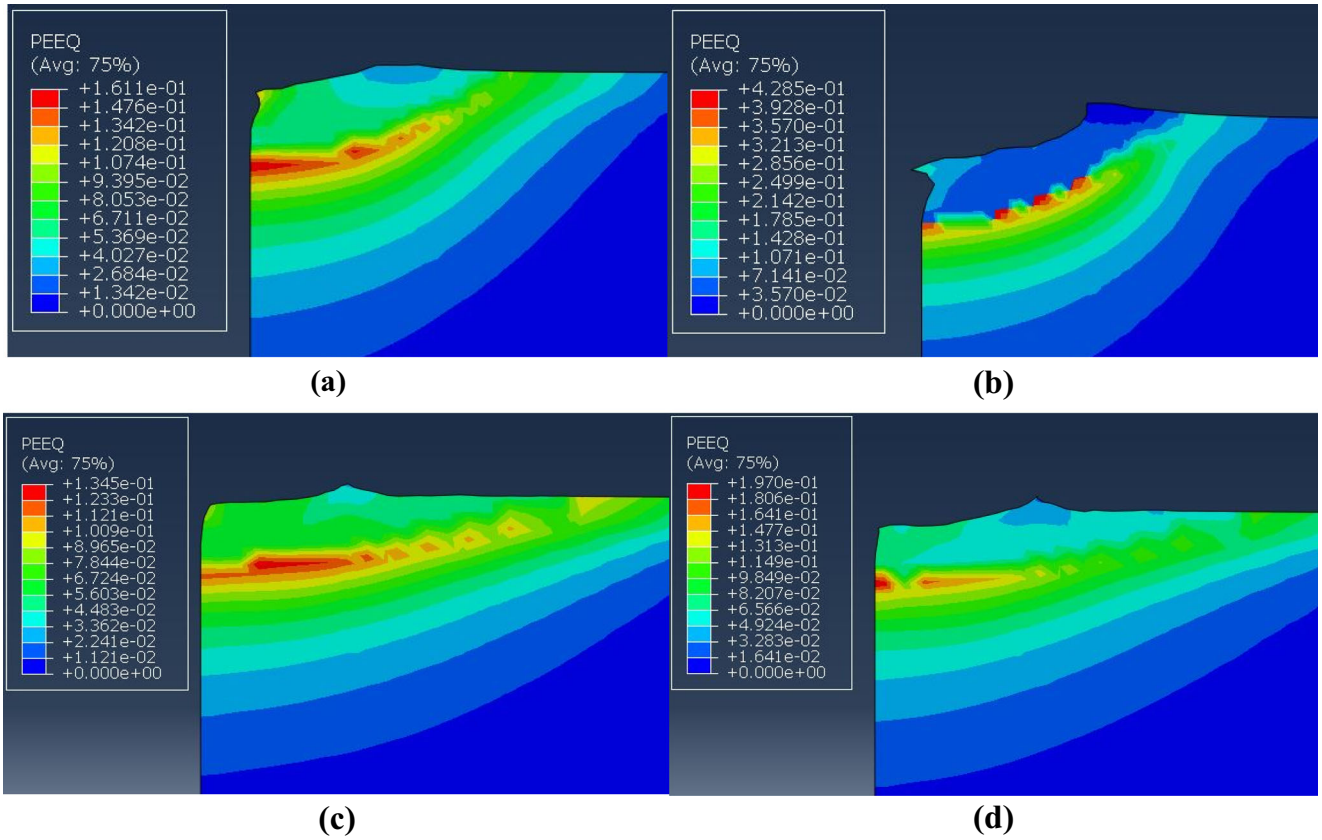


**Fig. 18** Equivalent plastic strain fields after total cooling in the case of thermal and pressure loading. Combinations: **a** C2, **b** C3, **c** C5, and **d** C6

compressive stress is observed. The numerical profile of the C4 combination, based on a GHFD, lies outside the error limits of the experimental measurements.

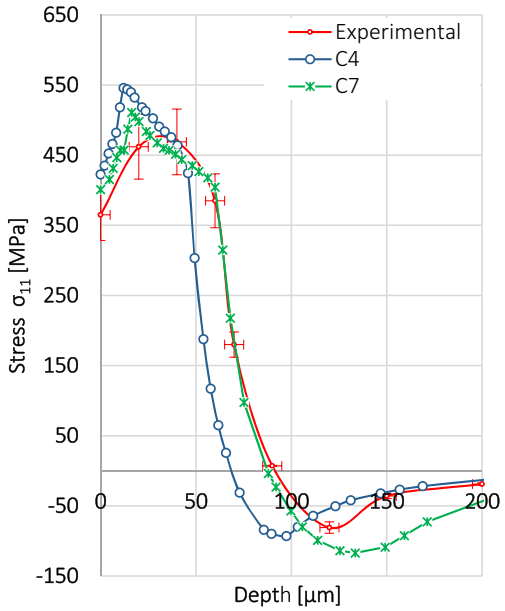


**Fig. 19** In-depth profiles of experimental and computed residual stress on 316L steel. Only thermal loading is considered. Combinations—C4: GHFD and C7: UHFD

#### 4.2.2 Influence of the pressure pulse

Figure 20 shows the in-depth residual-stress for the C2, C3 and C4 combinations. It can be noted that the addition of pressure does not change the overall shape of the numerical profiles, which mostly remain similar. For the same thermal loading, adding pressure did not improve the numerical prediction of the residual stresses. Profile C4, corresponding to a pure thermal load, almost coincides with profile C2 corresponding to the same thermal loading and a peak pressure of 3.33 GPa. Raising the pressure further increases the gap between the numerical and experimental profiles, which is clear for the combination C3 corresponding to a peak pressure of 5 GPa. The same tendency was also found for the combinations C5 and C6 (Fig. 21) where the pressure did not induce a positive effect on the accuracy of the residual stresses computation.

The form of the pressure-distribution did not show a significant influence on the residual stresses profile (Fig. 22). The profile of the combination C1, with Spherical Pressure-Distribution (SPD), is as close to the experimental profile as that of the combination C2 with Uniform Pressure-Distribution (UPD), despite its peak pressure (3.33 GPa) that was 250% more intense than that of the combination C1 (1.33 GPa).

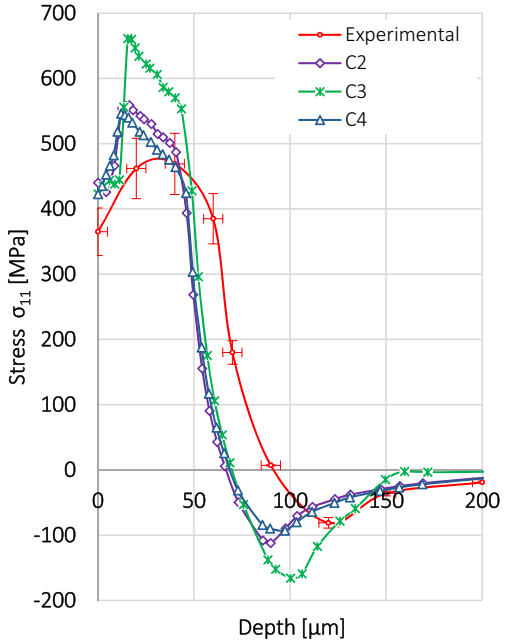


**Fig. 20** Effect of the pressure pulse on the computed residual stresses in the case of a GHFD. Combinations: C2, 3.33 GPa; C3, 5 GPa; and C4, 0 GPa

In this study we did not go beyond 1.33 GPa for the SPD case because, this form of distribution causes critical distortions in the mesh and beyond this limit the solver does not converge since no remeshing step is planned. This problem is seldom met in the case of a UPD even with peak pressure of 5 GPa. For this reason, the SPD was abandoned and only the results of the UPD are presented in the following.

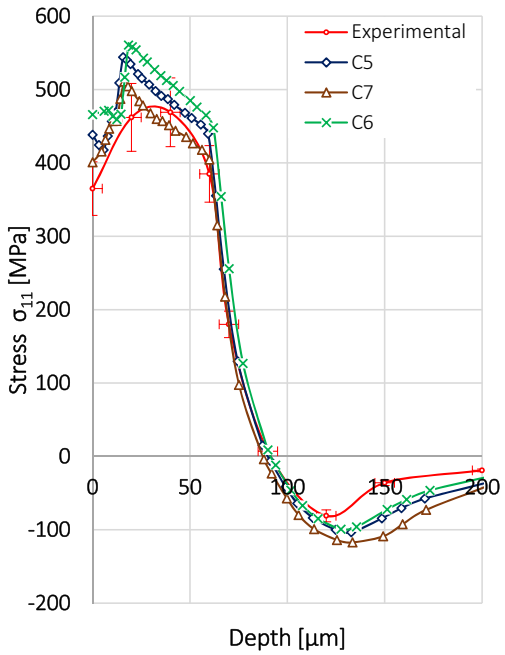


**Fig. 21** Effect of the pressure pulse on the computed residual stresses in the case of a UHFD. Combinations: C5, 2.46 GPa; C6, 3.7 GPa; and C7, 0 GPa

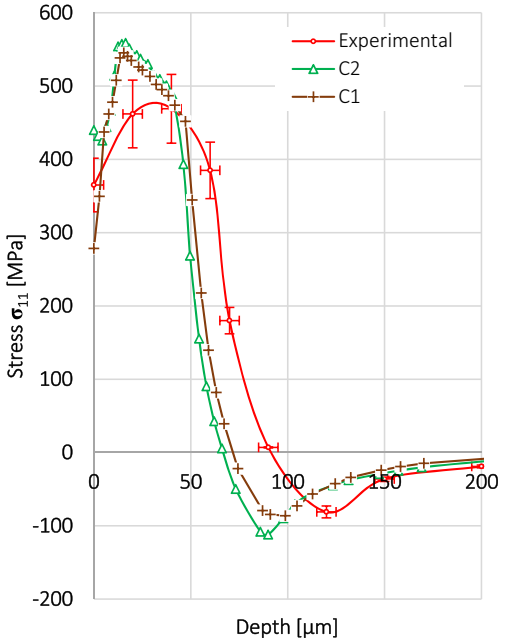


**Fig. 22** Effect of the pressure distribution form on computed residual stress. Combinations—C1: spherical and C2: uniform

### 4.3 Equivalent plastic strain validation

The EPS is sparsely sensitive to the HFD, as shown in Fig. 23. The maximum value, about 11.3%, was reached by both types of HFD at almost the same depth. However, the thickness of the plasticized zone due to the UHFD was about 100 versus 70 µm for the GHFD. The addition of the pressure as a load, increased the level of the plastic deformation and the thickness of the plasticized zone for the GHFD as confirmed by the Fig. 24. The EPS level increased from 11.3% for a pure thermal load (combination

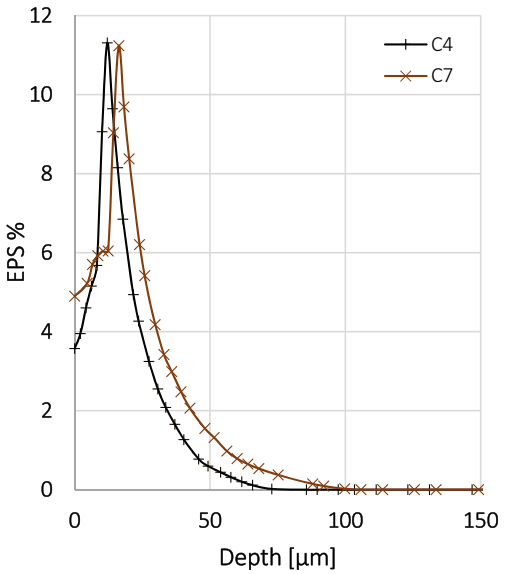


**Fig. 23** Comparison of computed EPS profiles in the case of pure thermal load. Combinations—C4: GHFD and C7: UHFD

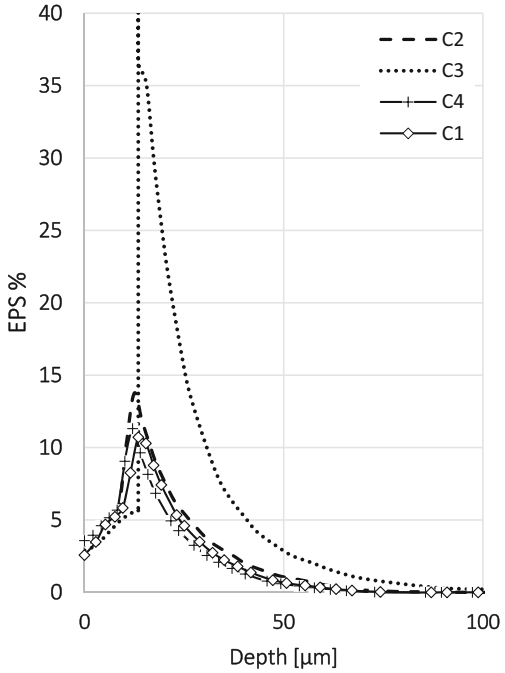


**Fig. 24** In-depth EPS computed in the case of GHFD

C4) to 40% in the case of a 5 GPa peak pressure (combination C3), a gain of 254%. The thickness of the plasticized area grew from 70 µm for the C4 combination to 100 µm for the C3 combination.

In the case of a UHFD, the addition of pressure mainly affected the level of the EPS. This latter increased proportionally with the applied peak pressure (Fig. 25). The EPS rose from 11.24% for a pure thermal load (combination C7) to 19.7% in the case of 3.7 GPa peak pressure (combination C6), a gain of 75.27%. The thickness of the plasticized zone seemed insensitive to the peak pressure level in the case of UHFD.

A qualitative comparison of computed and measured EPS was carried out as shown in Fig. 26. The experimental profile was obtained in correlation with the measurements of microhardness as explained earlier and the numerical profile is that resulting from the combination C3 since it caused the most intense EPS.

According to Fig. 26, the computed EPS profile is much lower than the experimental one with a shift of about 30% EPS. However, the numerical model provides a reasonable prediction of the 15 µm depth where the maximum amplitude of EPS is located and the thickness of the layer disturbed by the electrical discharge of approximately 100 µm.

## 5 Discussion

We have proposed in this study a numerical approach based on robust models more appropriate to the real physics that governs the EDM process in order to better understand the mechanical response of the workpiece during and after an electric discharge on which the EDM process is based. We intentionally focused on the latest electric discharges that occur at the end of a machining phase. More specifically, the discharges that condition the final mechanical state which is often qualified by residual.

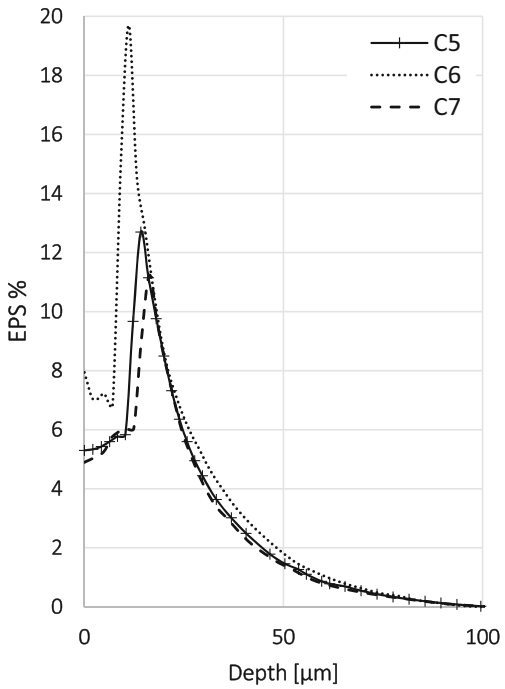


**Fig. 25** In-depth EPS computed in the case of UHFD

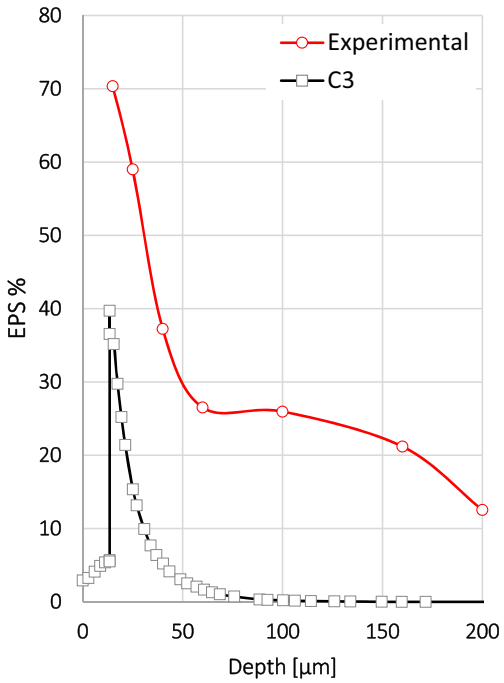


**Fig. 26** Comparison of experimental and computed in-depth EPS profiles

The mechanical problem is strongly coupled to the thermal problem, and the accuracy of the numerical results are directly related to the robustness of the thermal model. In fact, the thermal model depends on several parameters, including mainly the shape of the heat-flux distribution, the expansion of the heat source, and the amount of the energy $F_c$ transferred to the workpiece. It was therefore essential to investigate each of these parameters.

Given the diversity of the models, a strategic decision was made to deal with two kinds of heat-flux distributions: Gaussian and uniform with their respective values of $F_c$: 18 and 45%. Two models were selected to simulate the expansion of the heat source; one is of equivalent heat source type, and the other is of plasma expansion type.

Besides the thermal loading, a new boundary load was taken into account as an external pressure pulse applied in conjunction with the heat flux on the same boundary. The evidence of this pressure and its background are more and more cited in recent literature. This raises the need to initiate a first attempt to model plasma-induced pressure and to investigate its possible impact on the state of residual stresses and work hardening.

The mechanical behavior law is essential to enhance the reliability of the results. It was carefully designed so that it is well adapted to the very high strain rates that arise in the surface layers during the electrical discharges and even afterwards.

Several combinations of hypotheses were tested through numerical simulations in the case of a single electrical discharge. Therefore, the number of results was very high, so only the combinations that led to some conclusive results are presented and discussed.

It should be noted that the model referenced Eq. (7) governing the expansion of the heat source led to low and unacceptable temperatures, as they did not exceed 442 °C on the upper surface. In fact, this model caused premature expansion of the heat source that rapidly reached high radius values, which drastically reduced the heat-flux density. Consequently, this model was later abandoned.

In general, the selected models have demonstrated their ability to properly simulate the mechanical behavior of the EDMed layer during and after an electrical discharge. The comparison of the numerical and the experimental profiles of residual stresses revealed that the assumption of the uniform distribution of the heat flux is more precise than the Gaussian distribution in approximating the experimental measurements. Indeed, for the same expansion model of the heat source (Eq. 6), the Gaussian distribution model, concentrates the maximum of the heat flux power in a very narrow section around its axis. Far from the axis, the intensity of the heat flux decreased exponentially to almost zero at the heat source border. Contrariwise, with the uniform distribution, the heat flux was evenly distributed over the loaded section, which ensures a deeper penetration of the heat, even with a lower heat flux power (− 45.3%) compared with that used with the Gaussian distribution.

According to the modeling proposed in this study, the addition of a uniformly distributed pressure, as a loading condition, did not affect significantly the residual stress state that appeared to be substantially driven by the thermal loading more than by the pressure pulse. On the other hand, the effect of the pressure was particularly perceptible on the strain hardening and the crater morphology, and more precisely on the formation of a bulge around the crater due to the repelling phenomenon driven by the pressure and the superficial thermal expansion gradient.

In fact, during the electric discharge, a fraction of the material melted due to the very high temperatures caused by the plasma and formed a molten pool with a radius of about 14 μm. The stresses and strains were almost zero in this liquid area and appeared in the solid layer surrounding the molten pool. The existence of the pressure over the molten pool prevented its free expansion at the surface. This phenomenon was even more pronounced as the pressure was more intense. Thus confined, the incompressible liquid material further presses the underlying solid sublayers by transmitting to them a fraction of the pressure exerted on it, which increases the strain and the work hardening in these solid layers. The other fraction is dissipated in the bulge formation.

Once the electric discharge collapsed, the cooling phase began free of any external pressure. The shrinkage rate is the main phenomenon that governs the genesis and the evolution of stresses and strains in the molten pool and so on in the already prestressed solid sublayers. This may explain why in the near-surface layer of about 14 μm thick, the amplitudes of the residual stresses were fairly close for all the combinations studied. It is furthermore understood why the maximum amplitudes of the stresses and the work hardening are localized in sublayers. More precisely, in the solid boundary that was underlying the molten pool and which kept a memory of the work hardening and the thermal stresses formed rather during the heating phase and potentially amplified by the pressure that was applied.

The spherical distribution of the pressure has not been acutely investigated because of the critical distortions in the mesh, particularly at the surface. With this kind of distribution, it was impossible to exceed 1.33 GPa. A value for which the computed residual stresses were interesting as shown in (Fig. 22). Nevertheless, the level of work hardening remains similar to that caused by the pure thermal loading of the combination C4.

According to the modeling approach proposed in this study, the work hardening in the EDMed layer is caused by the thermal expansion and the applied pressure, at least in the deep zone. But, for all the combinations studied, the numerical results showed a work hardening level that is much lower than the experimental measurements.

The change of the chemical composition of the surface layer due to the diffusion of numerous chemical elements coming from the dielectric fluid and the tool material cannot stand alone to explain the high work hardening level, particularly in the deep layers. Moreover, the analyses made by EDS spectroscopy showed that the change of the carbon content did not exceed the first 10 μm below the machined surface. This suggests that other phenomena are potentially associated and manage the shift, such as microstructural changes caused by thermal cycles, and the cyclic hardening phenomenon that characterizes the 316 L steel [71], subsequent the perpetual electrical discharges that bombard the surface of the workpiece and cause untold numbers of thermal and mechanical loading cycles.

## 6 Conclusion

A new numerical approach is proposed in this study to get further insights into some aspects of the mechanical behavior of a workpiece of 316 L steel material subjected to an EDM basic electrical cycle. Several hypotheses have been assumed and investigated, including the shape of the heat flux distribution, the model of the heat-source expansion and the fraction of the energy transferred to the workpiece.

We attempted to develop a consistent model of the EDM plasma-induced pressure phenomenon that has been assumed as a new boundary load. The models adopted were coded and simulated with the commercial code Abaqus® and the obtained results led to the following conclusions:

- The proposed modeling and the adopted approach demonstrated their efficiency and ability to predict, as expected, the evolution of the mechanical behavior of the EDMed layer, since the set-up of the electric discharge and up to the total cooling of the workpiece;
- The combination made-of the uniform distribution of the heat flux, $F_c = 45\%$, and Eq. (6) as the heat-source expansion model was the most appropriate to approximate the real residual stress profile;
- As modeled in this study, the pressure effect is evident on the work hardening and the bulge formation and less obvious on the residual stresses;
- The plastic deformations induced by the thermal expansion and the pressure are insufficient to explain the high hardening level of the deep layers;
- The strain rate in the EDMed layer remains very high throughout the heating phase and even at the beginning of the cooling phase;
- The peak of the residual tensile stresses is located in the sublayer, at the earlier solid-liquid boundary. A local material decohesion might probably occur in this zone;
- The relaxation of the residual stresses on the surface layer is not only due to the damage;
- The assumptions on which the plasma-induced pressure modeling is based require further investigation and development to better clarify and quantify the potential mechanical effects of this phenomenon.



## References

1. McGeough JA, Rasmussen H (1982) A macroscopic model of electro-discharge machining. Int J Mach Tool D R 22:333–339. https://doi.org/10.1016/0020-7357(82)90010-5
2. Rizvi SAH, Agarwal S (2016) An investigation on surface integrity in EDM process with a copper tungsten electrode. Proc CIRP 42: 612–617. https://doi.org/10.1016/j.procir.2016.02.254
3. Ghanem F, Fredj NB, Sidhom H, Braham C (2011) Effects of finishing processes on the fatigue life improvements of electro-machined surfaces of tool steel. Int J Adv Manuf Technol 52: 583–595. https://doi.org/10.1007/s00170-010-2751-y
4. Ghanem F, Sidhom H, Braham C, Fitzpatrick ME (2002) Effect of near-surface residual stress and microstructure modification from machining on the fatigue endurance of a tool steel. J Mater Eng Perform 6:631–639. https://doi.org/10.1361/105994902770343629
5. Ekmekci B (2007) Residual stresses and white layer in electric discharge machining (EDM). Appl Surf Sci 253(23):9234–9240. https://doi.org/10.1016/j.apsusc.2007.05.078
6. Yadav V, Jain VK, Dixit PM (2002) Thermal stresses due to electrical discharge machining. Int J Mach Tool Manu 42:877–888
7. Meenakshi SM, Swee-Hock Y (2005) Process simulation and residual stress estimation of micro-electrodischarge machining using finite element method. Jpn J Appl Phys 44(7R):5254–5263. https://doi.org/10.1143/JJAP.44.5254
8. Das S, Klotz M, Klocke F (2003) EDM simulation: finite element-based calculation of deformation, microstructure and residual stresses. J Mater Process Technol 142:434–451. https://doi.org/10.1016/S0924-0136(03)00624-1
9. Rebelo JC, Kornmeier M, Batista AC, Dias AM (2002) Residual stress after EDM-FEM study and measurement results. Mater Sci Forum 404-407:159–164. https://doi.org/10.4028/www.scientific.net/MSF.404-407.159
10. Ekmekci B (2002) Theoretical and experimental investigation of residual stresses in electrical discharge machining. Ph.D. thesis, The Middle East Technical University
11. Ekmekci B, Tekkaya AE, Erden A (2006) A semi-empirical approach for residual stresses in electric discharge machining (EDM). Int J Mach Tools Manuf 46:858–868. https://doi.org/10.1016/j.ijmachtools.2005.07.020
12. Saeki T, Kunieda M, Ueki M, Satoh Y, Division AHT, Division AFE (1996) influence of joule heating on EDM processes of high-electric-resistivity materials. Paper presented at the ASME international mechanical congress and exposition, Atlanta
13. Pradhan MK (2010) Modeling and simulation of thermal stress in electrical discharge machining process. In: Proc. of the 4th international conference on advances in mechanical engineering, September 23–25, India, 2010
14. Ekmekci B, Elkoca O, Erman Tekkaya A, Erden A (2005) Residual stress state and hardness depth in electric discharge machining: de-

ionized water as dielectric liquid. Mach Sci Technol 9(1):39–61. https://doi.org/10.1081/MST-200051244
15. Shabgard M, Seydi S, Seyedzavvar M (2015) Novel approach towards finite element analysis of residual stresses in electrical discharge machining process. Int J Adv Manuf Technol 82(9–12): 1805–1814. https://doi.org/10.1007/s00170-015-7510-7
16. Srinivasa Rao P, Ramji K, Satyanarayana B (2016) Effect of wire EDM conditions on generation of residual stresses in machining of aluminum 2014 T6 alloy. AEJ 55(2):1077–1084. https://doi.org/10.1016/j.aej.2016.03.014
17. Liu JF, Guo YB (2016) Residual stress modeling in electric discharge machining (EDM) by incorporating massive random discharges. Proc CIRP 45:299–302. https://doi.org/10.1016/j.procir.2016.02.060
18. Mohanty CP, Sahu J, Mahapatra SS (2013) Thermal-structural analysis of electrical discharge machining process. Procedia Engineer 51:508–513. https://doi.org/10.1016/j.proeng.2013.01.072
19. Soni PK and Gholley R (2007) Study and analysis of residual stresses in electro-discharge machining (EDM). Btech thesis
20. Pérez R, Carron J, Rappaz M, Wälder G, Revaz B, Flükiger R (2007) Measurement and metallurgical modeling of the thermal impact of EDM discharges on steel. Paper presented at the 15th international symposium on electromachining, ISEM XV, pp 17–22
21. Ghanem F, Braham C, Sidhom H (2003) Influence of steel type on electrical discharge machined surface integrity. J Mater Process Technol 142:163–173. https://doi.org/10.1016/S0924-0136(03)00572-7
22. Salah Nizar B, Ghanem F, Atig Kaïs B (2008) Thermal and mechanical numerical modelling of electric discharge machining process. Commun Numer Methods Eng 24(12):2021–2034. https://doi.org/10.1002/cnm.1091
23. Guo J, Zhang G, Huang Y, Ming W, Liu M, Huang H (2014) Investigation of the removing process of cathode material in micro-EDM using an atomistic-continuum model. Appl Surf Sci 315:323–336. https://doi.org/10.1016/j.apsusc.2014.07.130
24. Yang X, Han X, Zhou F, Kunieda M (2013) Molecular dynamics simulation of residual stress generated in EDM. Proc CIRP 6:432–437. https://doi.org/10.1016/j.procir.2013.03.037
25. Yang X, Guo J, Chen X, Kunieda M (2011) Molecular dynamics simulation of the material removal mechanism in micro-EDM. Precis Eng 35(1):51–57. https://doi.org/10.1016/j.precisioneng.2010.09.005
26. Zhang G, Guo J, Ming W, Huang Y, Shao X, Zhang Z (2014) Study of the machining process of Nano-electrical discharge machining based on combined atomistic-continuum modeling method. Appl Surf Sci 290:359–367. https://doi.org/10.1016/j.apsusc.2013.11.084
27. Singh A, Ghosh A (1999) A thermo-electric model of material removal during electric discharge machining. Int J Mach Tools Manuf 39(4):669–682. https://doi.org/10.1016/s0890-6955(98)00047-9
28. Yue X, Yang X (2017) Molecular dynamics simulation of single pulse discharge process: clarifying the function of pressure generated inside the melting area in EDM. Mol Simul 43(12):935–944. https://doi.org/10.1080/08927022.2017.1306649
29. Yue X, Yang X (2016) Study on the distribution of removal material of EDM in deionized water and gas with molecular dynamics simulation. Proc CIRP 42:691–696. https://doi.org/10.1016/j.procir.2016.02.303
30. Hayakawa S, Kusafuka Y, Itoigawa F, Nakamura T (2016) Observation of material removal from discharge spot in electrical discharge machining. Proc CIRP 42:12–17. https://doi.org/10.1016/j.procir.2016.02.175
31. Peyre P, Chaieb I, Braham C (2007) FEM calculation of residual stresses induced by laser shock processing in stainless steels, modelling Simul. Mater Sci Eng 15:205–221. https://doi.org/10.1088/0965-0393/15/3/002
32. Song H (2010) Analyse expérimentale et numérique de la distribution des contraintes résiduelles induites par choc-laser dans les alliages d'aluminium. Sciences de l'ingénieur [physics]. Arts et Métiers ParisTech. Français. <NNT: 2010ENAM0002>. <pastel-00005901>
33. Belassel M (1994) Etude de la distribution des contraintes d'ordre I et II par diffraction des rayons X dans un acier perlitique, Thèse, École Nationale Supérieure d'Arts et Métiers de Paris
34. Sollier A (2002) Etude des plasmas générés par interaction laser-matière en régime confiné. Application au traitement des matériaux par choc laser. Thesis prepared within the University of Versailles Saint Quentin en Yvelines. Url: https://tel.archives-ouvertes.fr/tel-00089243
35. Zhang Y, Liu Y, Shen Y, Ji R, Li Z, Zheng C (2014) Investigation on the influence of the dielectrics on the material removal characteristics of EDM. J Mater Process Technol 214(5):1052–1061. https://doi.org/10.1016/j.jmatprotec.2013.12.012
36. Soldera F, Lasagni A, Mücklich F, Kaiser T, Hrastnik K (2005) Determination of the cathode erosion and temperature for the phases of high voltage discharges using FEM simulations. Comput Mater Sci 32:123–139. https://doi.org/10.1016/j.commatsci.2004.06.004
37. Daalder JE (1978) A cathode spot model and its energy balance for metal vapour arcs. J Phys D Appl Phys 11(12):1667–1682
38. Kitamura T, Kunieda M (2014) Clarification of EDM gap phenomena using transparent electrodes. CIRP Ann 63(1):213–216. https://doi.org/10.1016/j.cirp.2014.03.059
39. Rich JA (1961) Resistance heating in the arc cathode spot zone. J Appl Phys 32(6):1023–1031. https://doi.org/10.1063/1.1736153
40. Maradia U, Hollenstein C, Wegener K (2015) Temporal characteristics of the pulsed electric discharges in small gaps filled with hydrocarbon oil. J Phys D Appl Phys 48(5):055202. https://doi.org/10.1088/0022-3727/48/5/055202
41. Yeo SH, Kurnia W, Tan PC (2008) Critical assessment and numerical comparison of electro-thermal models in EDM. J Mater Process Technol 203(1–3):241–251. https://doi.org/10.1016/j.jmatprotec.2007.10.026
42. Tlili A, Ghanem F, Salah Nizar B (2015) A contribution in EDM simulation field. Int J Adv Manuf Technol 79(5–8):921–935. https://doi.org/10.1007/s00170-015-6880-1
43. Assarzadeh S, Ghoreishi M (2016) Electro-thermal-based finite element simulation and experimental validation of material removal in static gap single-spark die-sinking electro-discharge machining process. Proc Inst Mech Eng B J Eng Manuf 231(1):28–47. https://doi.org/10.1177/0954405415572661
44. Guo YB, Klink A, Klocke F (2013) Multiscale modeling of sinking-EDM with Gaussian heat flux via user subroutine. Proc CIRP 6:438–443. https://doi.org/10.1016/j.procir.2013.03.047
45. Allen P, Chen X (2007) Process simulation of micro electro-discharge machining on molybdenum. J Mater Process Technol 186:346–355. https://doi.org/10.1016/j.jmatprotec.2007.01.009
46. Kansal HK, Singh S, Kumar P (2008) Numerical simulation of powder mixed electric discharge machining (PMEDM) using finite element method. Math Comput Model 47(11–12):1217–1237. https://doi.org/10.1016/j.mcm.2007.05.016
47. Joshi SN, Pande SS (2010) Thermo-physical modeling of die-sinking EDM process. J Manuf Process 12(1):45–56. https://doi.org/10.1016/j.jmapro.2010.02.001
48. Tang J, Yang X (2016) A thermo-hydraulic modeling for the formation process of the discharge crater in EDM. Proc CIRP 42:685–690. https://doi.org/10.1016/j.procir.2016.02.302
49. Zhang Y, Liu Y, Shen Y, Li Z, Ji R, Cai B (2014) A novel method of determining energy distribution and plasma diameter of EDM. Int J

Heat Mass Transf 75:425–432. https://doi.org/10.1016/j.ijheatmasstransfer.2014.03.082
50. Kojima A, Natsu W, Kunieda M (2008) Spectroscopic measurement of arc plasma diameter in EDM. CIRP Ann 57(1):203–207. https://doi.org/10.1016/j.cirp.2008.03.097
51. Escobar AM, De Lange DF, Castillo HIM, Gutiérrez FGP (2013) Influence of modeling assumptions on the simulated EDM performance. In: Proceedings of the ASME 2013 international mechanical engineering congress & exposition IMECE2013
52. DiBitonto DD, Eubank PT, Patel MR, Barrufet MA (1989) Theoretical models of the electrical discharge machining process. I. A sample cathode erosion model. J Appl Phys 66(9):4095–4103. https://doi.org/10.1063/1.343994
53. Xia H, Kunieda M, Nishiwaki N (1996) Removal amount difference between anode and cathode in EDM process. International Journal of Electrical Machining 1:45–52
54. Singh H (2012) Experimental study of distribution of energy during EDM process for utilization in thermal models. Int J Heat Mass Transf 55(19–20):5053–5064. https://doi.org/10.1016/j.ijheatmasstransfer.2012.05.004
55. Revaz B, Emery J, Witz G, Flükiger R, Perez R, Carron J, Rappaz M (2005) Local temperature response to pulsed discharges in electronic discharge machining (EDM) environment. IEEE T Plasma Sci 33(3):1066–1071. https://doi.org/10.1109/TPS.2005.848611
56. Klocke F, Schneider S, Mohammadnejad M, Hensgen L, Klink A (2017) Inverse simulation of heat source in electrical discharge machining (EDM). Proc CIRP 58:1–6. https://doi.org/10.1016/j.procir.2017.03.178
57. Patel MR, Barrufet MA, Eubank PT, DiBitonto DD (1989) Theoretical models of the electrical discharge machining process. II. The anode erosion model. J Appl Phys 66(9):4104–4111. https://doi.org/10.1063/1.343995
58. Ikai T, Hashiguchi K (1995) Heat input for crater formation in EDM. Paper presented at the 11th international symposium for electromachining, ISEM 11; Lausanne; Switzerland,
59. Shankar P, Jain VK, Sundararajan T (1997) Analysis of spark profiles during EDM process. Mach Sci Technol 1(2):195–217. https://doi.org/10.1080/10940349708945647
60. Tariq Jilani S, Pandey PC (1982) Analysis and modelling of EDM parameters. Precis Eng 4(4):215–221. https://doi.org/10.1016/0141-6359(82)90011-3
61. Liu JF, Guo YB (2016) Thermal modeling of EDM with progression of massive random electrical discharges. Procedia Manufacturing 5:495–507. https://doi.org/10.1016/j.promfg.2016.08.041
62. International Atomic Energy Agency (2008) Thermophysical properties of materials for nuclear engineering: a tutorial and collection of data. IAEA, Vienna. ISBN 978-92-0-106508-7
63. Fousseny K (2012) Étude expérimentale, modélisation et simulation numérique de l'usinage à sec des aciers inoxydables: Étude de l'effet des revêtements mono et multi couches. Thesis prepared within the Laboratory LEMTA UMR CNRS 7563, University of Lorraine. October 2012. Publication authorized by the jury. URL: http://www.theses.fr/2012LORR0155
64. Dupas P, Waeckel F (1994) Recueil bibliographique de caractéristiques thermomécaniques pour l'acier de cuve, les revêtements inoxydables et les alliages 182 et 600, Rapport EDF/DER HI-74/93/097, HT-26/93/058A
65. Lionel D (2004) Simulation numérique du soudage–acier 316L validation sur cas tests de complexité croissante. Thesis prepared within the Laboratory of Research in Civil Engineering of the INSA, the national institute of applied sciences of Lyon. Id. No. 04 ISAL 0014. March 2004. Publication authorized by the jury
66. Sollier A (2002) Etude des Plasmas par Interaction Laser-matière en Régime Confiné. Application au Traitement des Matériaux par Choc-Laser, Thèse de doctorat, Université de Versailles, St. Quentin
67. Peyre P, Scherpereel X, Berthe L, Carboni C, Fabbro R, Béranger G, Lemaitre C (2000) Surface modifications induced in 316L steel by laser peening and shot-peening. Influence on pitting corrosion resistance. Mater Sci Eng A 280(2):294–302. https://doi.org/10.1016/S0921-5093(99)00698-X
68. Descoeudres A (2006) Characterization of electrical discharge machining plasmas. Thesis Swiss Federal Institute of technology EPFL, No. 3542. https://doi.org/10.5075/epfl-thesis-3542
69. Ning JI (1989) Application de l'Analyse des Profils de Raies de Diffraction X pour Caractériser l'Etat Microstructural et Mécanique des Matériaux Métalliques. Doctoral thesis Arts et Métiers ParisTech, France
70. Ben Moussa N, Sidhom H, Braham C (2012) Numerical and experimental analysis of residual stress and plastic strain distributions in machined stainless steel. Int J Mech Sci 64:82–93. https://doi.org/10.1016/j.ijmecsci.2012.07.011
71. Laamouri A, Sidhom H, Braham C (2013) Evaluation of residual stress relaxation and its effect on fatigue strength of AISI 316L stainless steel ground surfaces: experimental and numerical approaches. Int J Fatigue 48:109–121. https://doi.org/10.1016/j.ijfatigue.2012.10.008